Transformation of Co-containing birnessite to todorokite: Effect of Co on the transformation and implications for Co mobility

Zhongkuan Wu [a], Caroline L. Peacock [b], Bruno Lanson [c], Hui Yin [a], Lirong Zheng [d]
Zhongjun Chen [d], Wenfeng Tan [a], Guohong Qiu [a], Fan Liu [a,*], Xionghan Feng [a,*]

[a] Key Laboratory of Arable Land Conservation (Middle and Lower Reaches of Yangtse River) Ministry of Agriculture, College of Resources and Environment, Huazhong Agricultural University, Wuhan 430070, China
[b] School of Earth and Environment, University of Leeds, Leeds LS2 9JT, UK
[c] University of Grenoble Alpes, CNRS, ISTerre, F-38000 Grenoble, France
[d] Beijing Synchrotron Radiation Facility, Institute of High Energy Physics, Chinese Academy of Sciences, Beijing 100039, China

Abstract

The mobility and fate of bioessential transition metals, such as Ni and Co, are strongly controlled by their association with phyllomanganate minerals such as birnessite. These minerals however, can transform to tectomanganates such as todorokite during soil and sediment diagenesis, yet the mobility and fate of most metals during the transformation process remain largely unknown. Here this research investigates the effect of Co on, and the mobility and fate of Co during the transformation of birnessite into tunnel structure minerals. A range of Co-containing birnessite precursors with up to 16.9 % Co/(Co + Mn) molar ratios were synthesised, and subsequently transformed via a mild reflux procedure designed to mimic the diagenesis of these layered precursors into tunnel structures. The layered precursors and reflux products were characterized using a combination of mineralogical and geochemical techniques, including powder X-ray diffraction (XRD), Fourier transform infrared spectroscopy (FTIR), high resolution transmission electron microscopy (HRTEM) and extended X-ray absorption fine structure (EXAFS) spectroscopy. The results show that Co(III) is structurally incorporated into the layered precursors and reflux products, through the isomorphic substitution of Mn(III). The structural incorporation of Co(III) into the layered precursors leads to an overall reduction of Jahn-Teller distorted Mn(III) octahedra in these minerals, a key factor for their transformation to tunnel structures. As a consequence, the presence of such structural Co(III) disrupts the transformation of birnessite into todorokite, leading to the coexistence of 9.6 Å asbolane-like phyllomanganate and non-ideal $3 \times n$, or a-disordered, todorokite-like tectomanganates in the transformation products. Newly formed todorokite exhibits a wide range of $3 \times n$ tunnel dimensions (n up to 13) and a plate-like morphology. Overall the structural incorporation of non Jahn-Teller distorted cations like Co(III) into birnessite might help explain the often observed predominance of phyllomanganates over tectomanganates in soils and sediments, and the persistence of phyllomanganates in ferromanganese deposits that can be many millions of years old. The results also indicate that Co(III) initially associated with birnessite is retained in the solid phase during transformation, and thus the mobility of Co(III) is limited. EXAFS data suggest that Co is mainly located in the octahedral layers

* Corresponding authors.
  E-mail addresses: liufan@mail.hzau.edu.cn (F. Liu), fxh73@mail.hzau.edu.cn (X. Feng).

of asbolane-like phyllomanganate and at non-edge sites in non-ideal todorokite. Overall the transformation of Co-containing birnessite into non-ideal todorokite and asbolane-like layered structures maintains the strong sequestration of Co by Mn oxides.

1. INTRODUCTION

Natural Mn oxides encompass a variety of structural variants, most of them based on $Mn(III, IV)O_6$ octahedra sharing edges and/or corners (Post, 1999). These oxides are ubiquitous, occurring for example in soils, sediments and oceanic ferromanganese crusts and nodules (Taylor et al., 1964; Burns and Burns, 1975, 1977; Chukhrov et al., 1982; Murray et al., 1984; Post, 1999; Vodyanitskii et al., 2004). The coexistence of Mn(II/III/IV) within these oxides, and the related charge deficit that this creates, makes these oxides highly reactive, in particular with respect to the sorption and/or oxidation of transition metals (e.g., Manceau et al., 2002; Tebo et al., 2004; Webb et al., 2005; Peacock and Sherman, 2007a; Peacock, 2009) and the oxidative degradation of organic contaminants (Tebo et al., 2004; Remucal and Ginder-Vogel, 2014). The reactivity of these oxides is often reinforced by their micro- to nano-crystallinity, which provides them with large specific surface areas (Post, 1999; Lanson et al., 2000, 2002a,b). This strengthens their role as key players in the environmental fate of inorganic and organic nutrients and contaminants (e.g., Villalobos et al., 2005; Grangeon et al., 2012), but in turn often hampers their precise identification (Chukhrov et al., 1987; Post, 1999).

Two main families of Mn oxides may be differentiated, i.e. phyllomanganates and tectomanganates. Phyllomanganates are 2D minerals whose layers are built of edge-sharing MnO_6 octahedra. Layer charge deficit results either from isomorphic Mn(III)-for-Mn(IV) substitutions or from the presence of vacant layer sites. In the first instance, to minimize steric strains arising from the Jahn-Teller distortion of Mn(III) octahedra, these elementary blocks may be segregated into Mn(III)-rich rows in which the octahedra are systematically elongated along the same direction (the *a* axis). The induced cooperative Jahn-Teller effect then leads to an orthogonal layer symmetry ($a > \sqrt{3}b$), and the layer charge deficit is generally compensated for by the presence of protons, hydrated alkali or alkaline-earth cations (Drits et al., 1997, 2007; Silvester et al., 1997; Lanson et al., 2002a; Webb et al., 2005; Gaillot et al., 2007). In the second instance, the presence of vacant layer sites leads to a hexagonal layer symmetry ($a = \sqrt{3}b$), where the layer charge deficit is neutralized by interlayer cations such as H^+, K^+, and so on (Silvester et al., 1997; Manceau et al., 1997; Lanson et al., 2000; Villalobos et al., 2006; Bodeï et al., 2007; Drits et al., 2007; Peacock and Sherman, 2007b). The vacant layer sites also allow for the sorption of multi-valent cations as inner sphere complexes above/below these sites (triple corner sites: e.g.,

Post and Appleman, 1988; Manceau et al., 1997, 2002, 2004, 2007; Lanson et al., 2002b; Villalobos et al., 2005; Peacock and Sherman, 2007a,b; Grangeon et al., 2008; Peacock, 2009; Peña et al., 2010). In both orthogonal and hexagonal phyllomanganates, the layer-to-layer distance is ~7.0–7.2 Å (e.g. birnessite, vernadite, chalcophanite; Post and Appleman, 1988; Drits et al., 1997; Silvester et al., 1997; Lanson et al., 2000, 2002a,b). This distance may be increased to ~9.4–10.0 Å when interlayer alkali or alkaline-earth cations retain two planes of interlayer H_2O molecules (i.e. buserite) or when an additional octahedral brucite-like sheet is sandwiched between two Mn octahedral sheets (lithiophorite, asbolane; Chukhrov et al., 1982, 1987; Manceau et al., 1987; Post and Appleman, 1988, 1994; Post, 1999).

Tectomanganates are 3D minerals, in which chains of edge-sharing MnO_6 octahedra share corners, thus leading to "tunnel" structures. Nomenclature of the natural tunnel oxides relies essentially on the $n \times m$ tunnel size, with ideal pyrolusite, cryptomelane and todorokite having 1×1, 2×2 and 3×3 tunnel sizes, respectively, and on the nature of the cations present within these tunnels. It is commonly accepted that tectomanganates originate from the transformation of phyllomanganate precursors (Burns and Burns, 1977; Golden et al., 1986; Ching et al., 1999; Feng et al., 1999; Shen et al., 2005; Bodeï et al., 2007; Cui et al., 2008, 2009, 2010; Grangeon et al., 2014, 2015; Atkins et al., 2014). For example, todorokite, that exhibits intense diffraction lines at 9.6 Å and 4.8 Å (JCPDS 38-0475), may be prepared by heating Mg-exchanged buserite either in an autoclave or at atmospheric pressure (Golden et al., 1986; Feng et al., 2004). As phyllomanganate precursors often have transition metals sorbed at their surface and/or incorporated within their octahedral layers, the fate of these elements during the phyllomanganate-to-tectomanganate conversion is of special interest for their geochemical cycling (e.g., Siegel and Turner, 1983; Atkins et al., 2014, 2016). Experimental investigations of the mobility and fate of metals during todorokite formation from layered precursors however, show mixed results, with studies reporting both the incorporation of metal ions into the framework of newly formed todorokite (Yin et al., 1994; Ching et al., 1999; Nicolas-Tolentino et al., 1999; Kumagai et al., 2005; Onda et al., 2007) or the loss of metal ions from precursor birnessite with only the surface adsorption of metal ions onto newly formed todorokite (Atkins et al., 2016).

In this context, the fate of Co during the transformation of layered precursors is of special interest owing to its high natural affinity for layered Mn oxides. Early observations showed that layered Mn minerals present in Australian soils (birnessite and lithiophorite) contain relatively large

amounts of Co with Co/(Co + Mn) molar ratios of ∼0.01–0.02 (Taylor et al., 1964; Taylor, 1968). Similarly, in mining district sediments Co concentration is also positively correlated with the content of Mn oxides (Fuller and Harvey, 2000; Dublet et al., 2017), which can exhibit Co/(Mn + Co) molar ratios up to 0.34 (asbolane; Manceau et al., 1987). This geochemical Mn-Co association is also recognized in the marine environment, where ferromanganese nodules and crusts composed predominantly of layered Mn oxides are enriched in Co relative to seawater (e.g., Murray, 1975; Burns and Burns, 1977; Murray and Dillard, 1979; Saito and Moffett, 2002). Monomineralic Co-containing layered Mn oxides, such as lithiophorite and asbolane, have been identified in soils, lateritic formations and oceanic ferromanganese nodules (Chukhrov et al., 1982, 1987; Ostwald, 1984; Llorca, 1987, 1988; Manceau et al., 1987, 1992). Coupled with Co sorption, layered Mn oxides are also able to oxidize Co(II). The oxidation of Co(II)-to-Co(III) by birnessite was first revealed using X-ray photoelectron spectroscopy (Murray and Dillard, 1979), and later shown to be initiated at the edges of birnessite particles (Simanova and Peña, 2015). A combination of polarized extended X-ray absorption fine structure (EXAFS) spectroscopy and X-ray diffraction (XRD) shows that both layer and interlayer Mn(III) can oxidize Co(II) and lead to Co(III) migration into the octahedral layers (Manceau et al., 1997; Yu et al., 2012). Both Co(II) oxidation and the subsequent migration of Co(III) into the mineral structure appear to be key to the high capacity of layered Mn oxides for Co scavenging (Yin et al., 2014) and their resulting Co-enrichment (Loganathan and Burau, 1973; Davies and Morgan, 1989). As Co(III)O$_6$ octahedra are not Jahn-Teller distorted, Co-enrichment in birnessite layers may modify layer symmetry from orthogonal to hexagonal (Yin et al., 2015). This enrichment may also impact the ability of Co-containing phyllomanganates to transform into tectomanganates as the abundance of distorted Mn(III) octahedra within the octahedral layers appears to be a key factor for the formation of tunnel structures (Burns et al., 1985; Bodeï et al., 2007; Cui et al., 2008; Atkins et al., 2014, 2016; Grangeon et al., 2014, 2015; Zhao et al., 2015).

To the authors' knowledge only a handful of studies have investigated the transformation of Co-containing layered Mn oxides into tunnel structures (Ching et al., 1999; Kumagai et al., 2005; Onda et al., 2007; Song et al., 2010). As expected, Co(II) is oxidized to Co(III) in the layered precursors and then indirect observations indicate that a significant proportion of Co in the precursor can be structurally incorporated into the newly formed tunnel structures, by replacing Mn (Ching et al., 1999; Kumagai et al., 2005; Onda et al., 2007; Song et al., 2010). In particular, it is suggested that Co(III) primarily substitutes for Mn(III) at the edge sites (Mn2 and Mn4, Fig. 1) of the 3 × 3 tunnel structure (Song et al., 2010). However, the mechanism of Co retention and the extent to which precursor Co is retained in the newly formed products are still unclear, and thus the mobility and fate of Co during the birnessite to todorokite transformation are still unknown.

The present study explores the transformation of Co-containing layered Mn oxide precursors into tectomanganates, in order to investigate the effect of Co on, and the fate of Co during the transformation process. A combination of XRD, Fourier-transform infrared (FTIR) spectroscopy, nitric acid treatment and high-resolution transmission electron microscopy (HRTEM) are used to characterize the layered precursors and the transformation products, and determine the effect of Co on their structures. The effect of Co on the transformation process is investigated and the key parameters leading to the formation of layered vs. tunnel structures are determined. These techniques are then combined with X-ray absorption near-edge structure (XANES) and EXAFS spectroscopy to examine the Mn and Co crystal chemistry in the layered precursors and transformation products, in order to better understand the ultimate fate of Co during layered Mn oxide transformation.

2. EXPERIMENTAL METHODS

2.1. Synthesis of layered precursors and transformation products

A number of different Co-containing layered precursors (birnessite) and transformation products were prepared
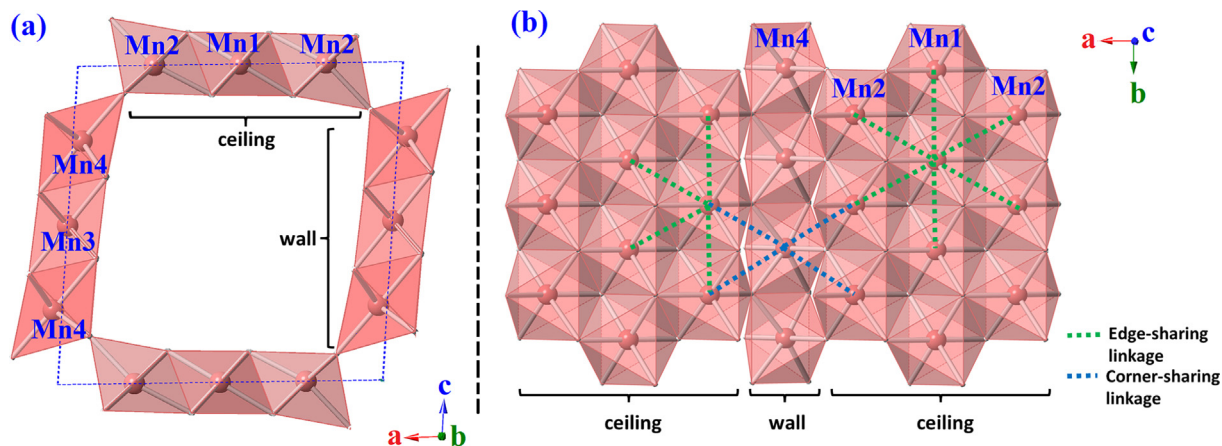

Fig. 1. Crystal structure of todorokite with a 3 × 3 tunnel size observed along b^* (a) and c^* (b) direction.

after Feng et al. (2004) and Song et al. (2010), together with Co-free birnessite and todorokite reference materials. To prepare the layered precursors, 250 mL of 5.5 M NaOH solution (refrigerated for 5 h at 4 °C) was added quickly to a 200 mL solution containing 0.5 M (Mn(II) + Co(II)), as $MnCl_2$ and $CoCl_2$, in which the molar ratios of Co to (Mn + Co) were 0, 0.05, 0.10, 0.15 and 0.20. The mixed solution was then stirred vigorously for 5 h and aerated with 2 L/min O_2. Each precipitate was washed with deionized water until the conductivity was below 2 µS/cm and half of each precipitate was dried at 60 °C for 3 days, while the other half was used to prepare todorokite. Layered precursors with molar ratios of Co/(Mn + Co) of 0, 0.05, 0.10, 0.15 and 0.20 are named Bir, CoB5, CoB10, CoB15 and CoB20, respectively, and the Co-containing layered precursors are collectively referred to as CoB.

The transformation of the layered precursors into tectomanganates was achieved using a reflux process (Feng et al., 2004). Briefly, the wet layered precursor was dispersed in 400 mL of 1 M $MgCl_2$ solution, stirred for 12 h at room temperature, and then washed 3 times. The resulting wet slurry was re-suspended in 500 mL deionized water in a 1 L triangle flask connected to a glass condenser with an oil bath kept at 100 °C and stirred for 24 h. After cooling to room temperature, the reflux products were separated from the solution by filtration, washed 3 times with deionized water and dried at 60 °C for 3 days. Transformation products of Bir, CoB5, CoB10, CoB15 and CoB20 are named Tod, CoT5, CoT10, CoT15 and CoT20, respectively, and the Co-containing reflux products are collectively referred to as CoT.

After the reflux procedure and when the reflux solutions were at room temperature (23 °C), the conductivity of these solutions was measured with a LeiCi DDS-11A conductimeter. All solid samples were ground in an agate mortar to particle sizes below 100 micron mesh to perform measurements described in Section 2.2. The elemental composition of all solid samples was determined in triplicate via atomic absorption spectrometry (Varian AAS 240FS). Actual Co/(Mn + Co) mole ratios in the Co-containing birnessites and reflux products are shown in Table 1. Co K-edge X-ray absorption near edge structure (XANES) spectra that confirm the presence of Co(III) in the layered

precursors and reflux products are shown in Fig. S1 (Supplementary Information).

2.2. Characterization of layered precursors and reflux products

The mineralogy of all samples was determined by powder XRD, collected on a Bruker D8 Advance diffractometer with Cu Kα radiation (λ = 0.15418 nm), operated at 40 kV/40 mA and at a scan rate of 1 °/min with a 0.02 ° step. FTIR spectroscopy was also performed, using a Bruker VERTEX 70. Prior to spectra acquisition, samples were mixed with KBr in a 1:80 ratio and then pressed into transparent slices. Spectra were recorded over 4000–400 cm^{-1} with a resolution of 1 cm^{-1} and with an average of 64 scans per sample (Zhao et al., 2015). Because it can be difficult to distinguish tectomanganate from buserite, lithiophorite- or asbolane-like phases using XRD (e.g., Burns et al., 1983, 1985; Bodeï et al., 2007; Saratovsky et al., 2009; Feng et al., 2010) we also performed a non-reducing nitric acid wash. This acid wash removes exchangeable species present in the interlayers of phyllomanganates and the tunnels of tectomanganates and so together with XRD provides information on mineral composition and structure. Specifically, after the loss of exchangeable species the d-spacing of phyllomanganates decreases from ~10 Å to ~7 Å, while that of todorokite remains stable. The acid wash also removes sorbed species and therefore the composition of the wash solution provides information on the crystal chemistry of Mn and Co, for example, whether Co is sorbed or structurally incorporated. The acid wash was conducted by adding 0.1 g sample into 250 mL 1 M HNO_3 solution with moderate stirring at room temperature (20 °C). An aliquot of 5 mL of the mixtures was withdrawn at different time intervals and immediately filtered through a 0.22 µm membrane to investigate the release of Mg, Mn and Co, the contents of which were analyzed by atomic absorption spectrometry.

The specific surface area of the reflux products was determined by the Brunauer–Emmett–Teller (BET) method using an Autosorb-1 standard physical adsorption analyzer (Quantachrome Autosorb-1, JEDL-6390/LV). Briefly, 0.15 g of sample was degassed at 110 °C for 3 h under vacuum prior to N_2 adsorption. The micromorphology of the reflux products was imaged with HRTEM on a Jeol JEM2100F operated at 200 kV.

The Mn and Co local environments in the layered precursors and reflux products were investigated using Mn and Co K-edge EXAFS spectroscopy. Spectra were collected at room temperature on the 1W1B beamline of the Beijing Synchrotron Radiation Facility (BSRF). Data were recorded in transmission mode (Mn K-edge) or fluorescence yield mode (Co K-edge), and the spectrum of a metallic Mn or Co foil was acquired simultaneously in transmission mode as a reference for energy calibration, respectively. The EXAFS spectra were processed via Athena, and fit using Artemis (Ravel and Newville, 2006). The Mn spectra were fit in R-space (R+ΔR) from 1 to 4 Å (3.06–12.7 Å^{-1}), with an amplitude reduction factor (S_0^2) of 0.8 (Grangeon et al., 2010). The Co spectra were also

Table 1
Co wt% and Co mole ratio in layered precursors and reflux products.

Samples	Co wt%	Co/(Mn + Co) mol %
Bir	–	–
CoB5	1.97(2)	3.3
CoB10	4.70(5)	7.7
CoB15	7.55(4)	12.5
CoB20	9.84(7)	16.9
Tod	–	–
CoT5	2.05(4)	3.8
CoT10	4.46(6)	8.3
CoT15	6.81(8)	13.5
CoT20	9.26(12)	17.9

fit in R-space (R + ΔR) from 1 to 4 Å (3.2–11.5 Å^{-1}), with an amplitude reduction factor (S_0^2) of 0.973 (Yin et al., 2014, 2015). Both the Mn and Co K-edge fits used scattering paths calculated from Mn/Co atoms in the Mn2 site in todorokite (JCPDS 38-0475), which contains both edge- and corner-sharing linkages. The Mn K-edge EXAFS spectra were also fit in Athena to determine the proportions of 9.6 Å phyllomanganate and tectomanganate in the reflux products. To do this, linear combination fitting of Mn K-edge EXAFS spectra was performed from 3 to 12 Å^{-1}, using CoT5 and corresponding CoB as standard samples for Co-containing tunnel and layered structures.

The Mn average oxidation state (AOS) in the layered precursors and reflux products was determined by applying a linear combination fitting method to the Mn K-edge XANES data, that is specifically designed for the determination of Mn valence states in mixed-valent Mn oxides (the so-called Combo method; Manceau et al., 2012). The reference compounds used for Mn(II), Mn(III) and Mn (IV) were those used in the original study (Manceau et al., 2012; Table 1).

3. RESULTS

3.1. Mineralogy of layered precursors and reflux products

3.1.1. X-ray diffraction

Birnessite has basal reflections at ~7.2 Å (001) and ~3.6 Å (002) (see triclinic birnessite JCPDS 43-1456 and hexagonal birnessite JCPDS 23-1239), while for the equivalent layered precursor with an expanded interlayer these appear at ~9.6 Å (001) and ~4.8 Å (002) (see buserite JCPDS 32-1128). Both birnessite and buserite also have *hk* reflections/bands at ~2.4 Å and ~1.4 Å due to periodicities within the phyllomanganate layers. In common with ~9.6 Å phyllomanganate, the tectomanganate todorokite has peaks at ~9.6 Å (001/100), ~4.8 Å (002/200), ~2.4–2.5 Å (21–1)/(40–1) and (210), and ~1.4 Å (020) (see JCPDS 38-475). As such, it can be difficult to distinguish todorokite from ~9.6 Å phyllomanganate using XRD (e.g., Burns et al., 1983, 1985; Bodeï et al., 2007; Saratovsky et al., 2009; Feng et al., 2010). However, in contrast to ~9.6 Å phyllomanganate, todorokite has additional peaks at 2.21 Å (21–2), 1.95 Å (21–3), 1.73 Å (313) and 1.52 Å (21–5) (see JCPDS 38-475). In addition, when ~9.6 Å layered precursors and todorokite reflux products are mixed, the ~2.4 Å peak is prominent and the ~2.5 Å peak manifests as a splitting of the ~2.4 Å peak (Atkins et al., 2014).

The XRD pattern of Bir (Fig. 2a) is in good agreement with that of standard triclinic birnessite (JCPDS 43-1456). The patterns of the CoB samples are very similar to Bir over the low-angle region 5-30°2θ), but show significant differences in the high-angle region (30-85°2θ) as the (200), (201), (202), (31–1) and (31–2) reflections of triclinic birnessite at 35.7°, 40.1°, 48.7°, 62.9°, and 64.5° (2θ Cu Kα), respectively, are weak or absent (Fig. 2a). Cell parameters derived from Rietveld refinement (Fig. S2) show that unit-cell parameter *a* gradually decreases from 5.171 Å

(Bir) to 4.956 Å (CoB20), while other parameters remain stable. As a result, the *a*/*b* ratio decreases from 1.818 to 1.736 (Table 2). Taken together, these changes indicate that the layer symmetry of Bir, CoB5 and CoB10 is orthogonal (*a*/*b* > √3), while the layer symmetry of CoB15 and CoB20 is hexagonal (*a*/*b* ≈ √3), as reported in Yin et al. (2015). The orthogonal layer symmetry in Bir is associated with the substitution of Mn(III) (0.58 Å, low spin) for Mn(IV) (0.53 Å) (Manceau et al., 1997), and the systematic elongation of Jahn–Teller distorted Mn(III) octahedra parallel to the ***a**** axis (Gaillot et al., 2007). Here, hexagonal symmetry is likely caused by the replacement of Mn(III) by Co(III) in the layer, where the ionic radius of Co(III) (0.54 Å, low spin) is sufficiently similar to that of Mn(III) to allow isomorphic substitution (Yin et al., 2015). With an increase in Co content however, the peaks of the CoB samples shift to higher angles, compared to Bir, and this is enhanced in the high-angle region (Fig. 3a). This shift in the XRD peaks occurs because Co(III) has a smaller ionic radius compared to Mn(III).

The XRD pattern of Tod (Fig. 2b) is typical of todorokite with characteristic peaks at 2.21 Å (21–2), 1.95 Å (21–3), 1.73 Å (313) and 1.52 Å (21–5) (JCPDS 38-475). Natural todorokite can also display distinct peaks at ~7.0 Å (12-14°2θ) and ~4.3 Å (19–21.5°2θ) (Post et al., 2003; Bodeï et al., 2007; Manceau et al., 2007). These reflections include (10–1) (12.5°) and (101) (13.5°), and (20–1) (19.8°), (10–2) (20.1°), (201) (21.0°) and (102) (21.3°) (JCPDS 38-475). As shown in Fig. 4, these reflections are parallel to the ***b**** axis and connect the corner site of the todorokite structure with the center of the non-adjacent wall, or the diagonal corner site. As such, the geometry of these crystal planes can be used to represent the periodicity of ideal 3 × 3 todorokite tunnel size. The Tod XRD pattern exhibits a broad hump at ~7 Å and a shoulder at ~4.3 Å rather than distinct peaks, and Tod might therefore possess non-ideal 3 × n tunnel structure. The patterns of the CoT samples are very similar to that of Tod, but the broad hump at ~7 Å is very weak, and the shoulder at ~4.3 Å is weak or absent (Fig. 3b). The CoT samples might therefore exhibit fewer ideal 3 × 3 tunnels and more non-ideal 3 × n tunnels compared to Tod. Furthermore, in the CoT samples, the 2.39 Å peak is prominent and the 2.46 Å peak, whose intensity increases with increasing Co content, appears as a splitting of the 2.39 Å peak (Fig. 2b). This suggests that the reflux products contain a mixture of ~9.6 Å layered structures and todorokite-like tunnel structures (Atkins et al., 2014). With an increase in Co content, the high-angle peaks of the CoT samples shift to higher angles compared to Tod (Fig. 2b), while the low-angle peaks shift to lower angles and sharpen (Fig. 3c), consistent with previous reports (Song et al., 2010). These contrasting changes relative to Tod in the high- and low-angle regions of the CoT XRD patterns indicate that Co incorporation causes a shrinkage of the [MnO$_6$] octahedral sheets, but an expansion of the distances between tunnel walls or ceilings, and/or adjacent phyllomanganate layers (Grangeon et al., 2010). We do not observe any peaks attributable to other Co-containing phases in the layered precursors or the reflux products.
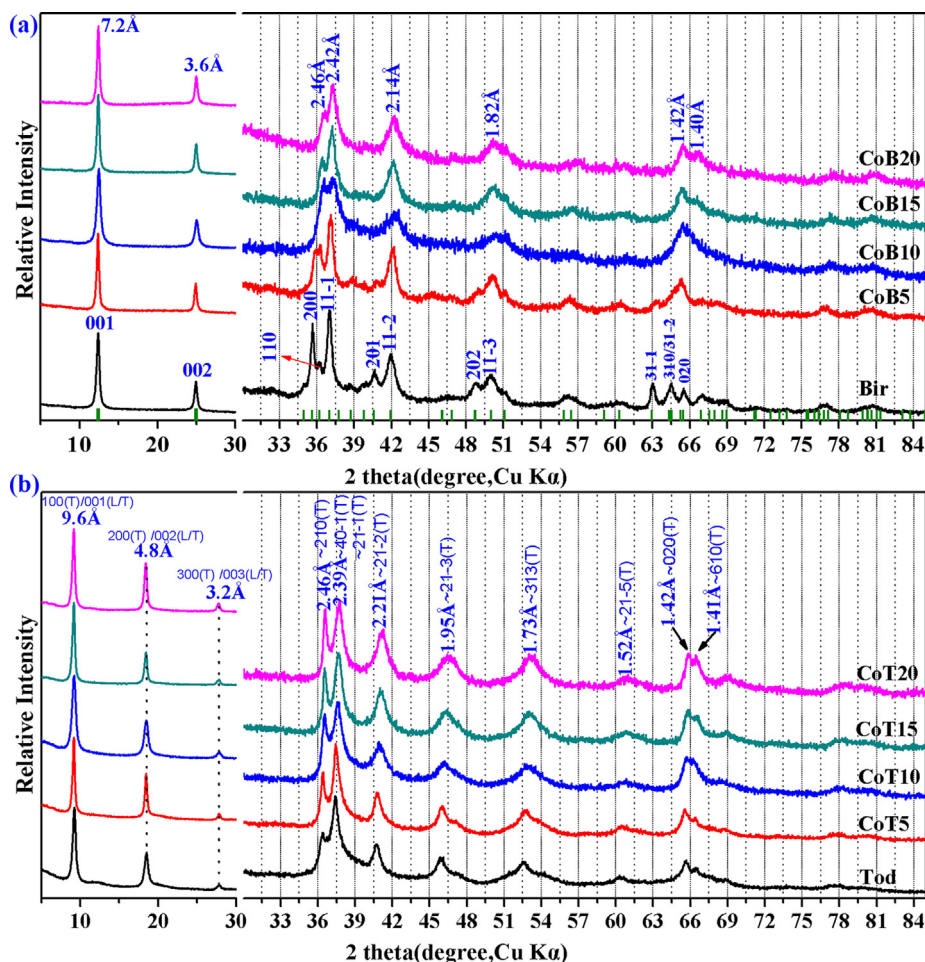
Fig. 2. Powder XRD patterns of layered precursors (a) and reflux products (b). Diffracted intensities peaks are normalized in the low and high angle region. Green ticks at the bottom of (a) indicate reflections of triclinic birnessite (JCPDS 43-1456). In (b), (L) and (T) indicate reflections of 9.6 Å layered Mn oxide and of todorokite (JCPDS 38-475), respectively. (For interpretation of the references to colour in this figure legend, the reader is referred to the web version of this article.)

Table 2
Lattice parameters derived from Rietveld refinements* for layered precursors.

Samples	a/Å	b/Å	c/Å	β/°	Rwp/%	a/b
Bir	5.1710(7)	2.8447(4)	7.3309(9)	103.37(2)	6.94	1.818
CoB5	5.1212(16)	2.8491(6)	7.3159(11)	102.65(3)	7.96	1.798
CoB10	5.0134(15)	2.8564(10)	7.2878(18)	101.95(6)	6.08	1.755
CoB15	4.9649(20)	2.8638(10)	7.2876(13)	102.07(4)	6.85	1.734
CoB20	4.9562(14)	2.8553(8)	7.2888(13)	102.30(4)	7.23	1.736

Note: Birnessite initial structural parameters were adapted from JCPDS 43-1456, and during the refinement process, cell parameters and site occupancy in the MnO_6 layer were refined. Co ions in CoB samples were assumed to substitute for Mn sites in the structure, such that the sum of occupation for Mn and Co was fixed to 1.

3.1.2. Fourier-transform infrared spectroscopy

In FTIR spectra of Mn oxides, the broad peak at ~761 cm^{-1} is attributed to the presence of an asymmetric Mn–O stretch from the triple chains of the todorokite lattice (Julien et al., 2004). This absorption band is therefore absent in phyllomanganates and tectomanganates with 1×1 or 2×2 tunnel sizes and is unique to both ideal (3×3) and non-ideal $(3 \times n, \ n > 3)$ todorokite (Julien et al., 2004). In agreement with XRD data, FTIR results show that all reflux products contain todorokite-like structures as evidenced by the presence of this peak at ~761 cm^{-1} (Fig. 5) (Julien et al., 2004; Atkins et al., 2014; Zhao et al., 2015). The intensity of this peak decreases with Co loading, however, suggesting that the proportion of todorokite-like structures in the reflux products decreases with increasing Co content.
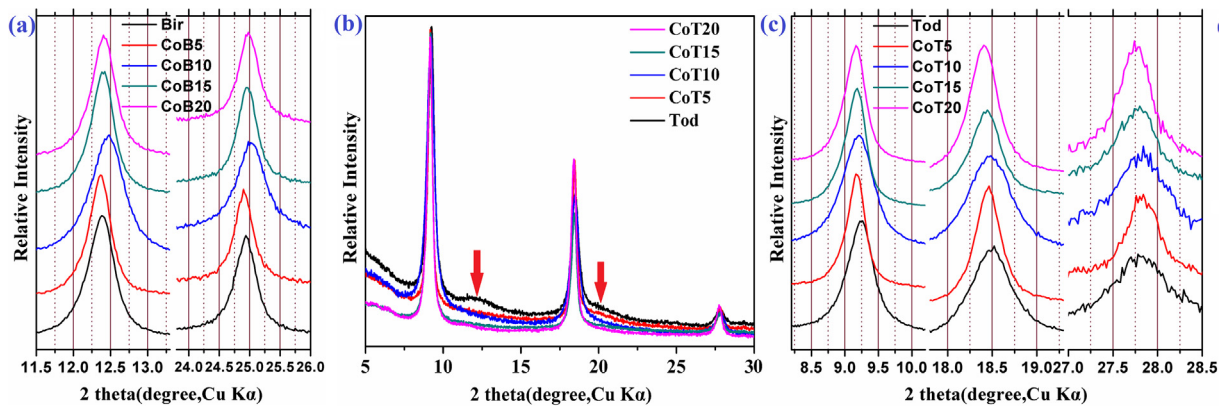
Fig. 3. Powder XRD patterns in the low angle region of the layered precursors (a), and the reflux products (b) and (c). Arrows in (b) indicate the broad hump and shoulder in the patterns.
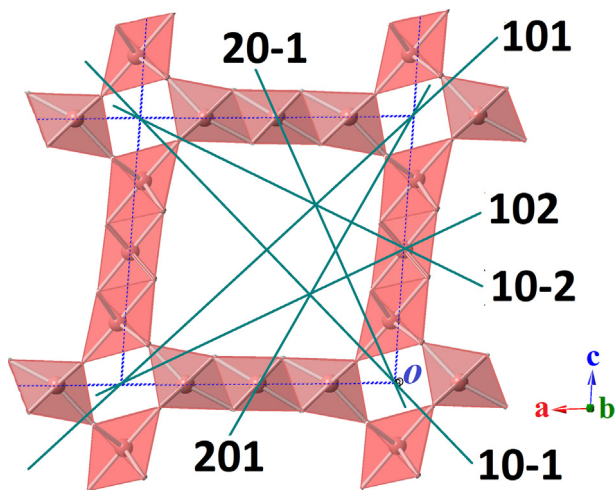

Fig. 4. Lattice planes of todorokite with a uniform 3×3 tunnel structure.

Fig. 5. FTIR spectra of layered precursors (bottom) and reflux products (top).

3.1.3. Nitric acid treatment

The XRD patterns (Fig. 6a) of the layered precursors after 1 M HNO_3 treatment for 1 week show reflections at ~2.33, 2.04, 1.72 Å and a more notable peak at 2.46 Å compared to the untreated samples, corresponding to the characteristic diffraction peaks of hexagonal birnessite (JCPDS 23-1239) (Lanson et al., 2000). These differences in the XRD patterns between the layered precursors before and after treatment are most likely related to mineralogical changes resulting from metal release into solution and/or the disproportionation of Mn(III) and its subsequent migration from layer to interlayer sites during the acid treatment. The concentrations of Mn, Co and Mg measured in solution during the acid treatment are shown in Fig. 7 as a fraction of their total content (Me_χ where Me = Mn, Co or Mg). The fraction of Mn released for all the layered precursors and reflux products is low (Fig. 7a and b) indicating that dissolution of the Mn oxide framework during the acid treatment is limited. As the acid treatment progresses, for each layered precursor, Mn_χ (Fig. 7a) is relatively constant and the final dissolved ratio is gener-
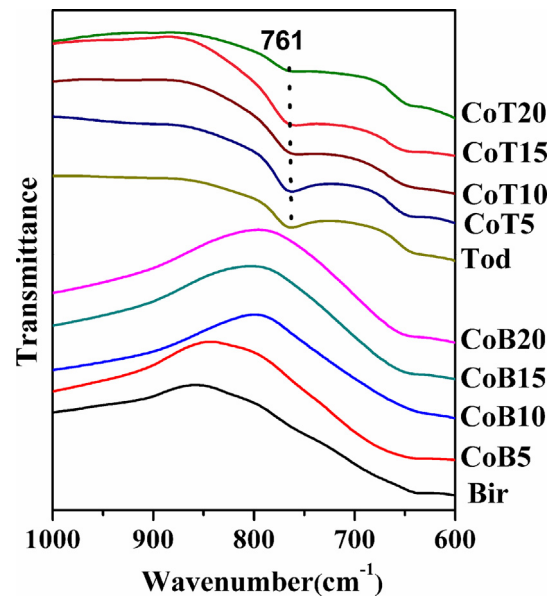
ally negatively correlated to the Co content in the samples. This negative correlation might be related to the amount of Mn that is sorbed, where, as Co content increases less Mn is sorbed and thus less Mn is readily removed during the acid treatment. This is potentially corroborated by the Mn AOS (Table 4) which show that as Co content increases there is reduced Mn(III) content. In contrast, Co_χ increases systematically with time (Fig. 7c), and Co_χ for CoB10, CoB15 and CoB20 are very similar during the entire treatment while Co_χ for CoB5 is markedly increased, compared to CoB10, CoB15 and CoB20. The limited release of Co from the CoB layered precursors suggests that Co is to a large extent structurally incorporated in the octahedral layers, and that the proportion of such incorporated Co increases with increasing Co content.

The XRD patterns of Tod and CoT5 (Fig. 6b) after being treated in 1 M HNO_3 for 1 week are not significantly different compared to the untreated samples, whereas
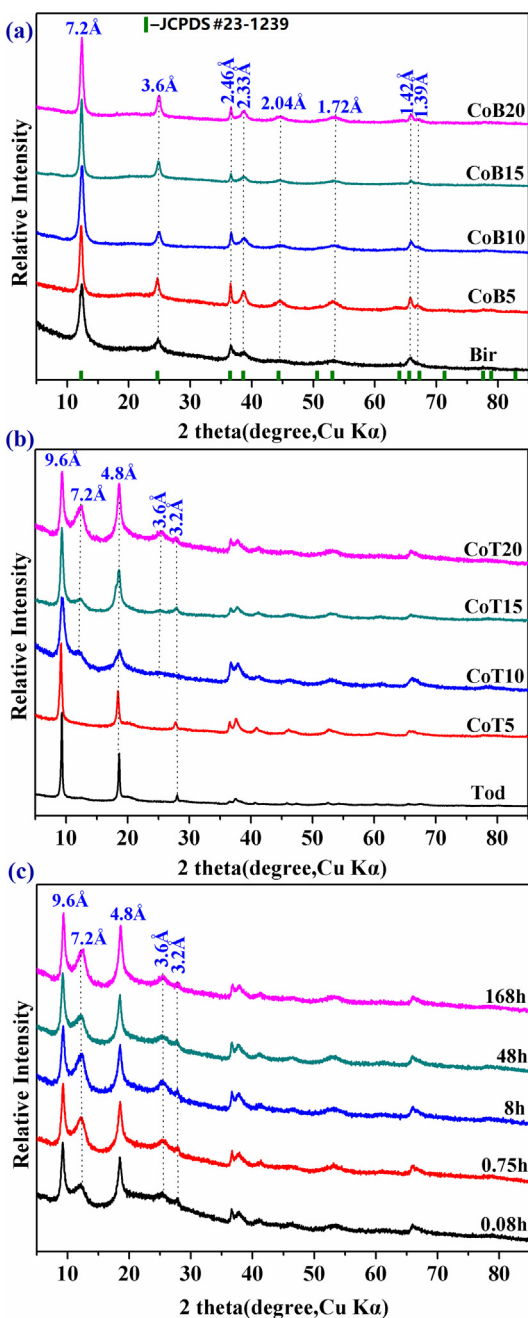
Fig. 6. XRD patterns of layered precursors and reflux products after nitric acid treatment: (a) layered precursors; (b) reflux products; (c) sample CoT20 after different nitric acid treatment durations.

CoT10, CoT15 and CoT20 show additional peaks at $\sim$7.2 Å and $\sim$3.6 Å, characteristic of birnessite, the intensity of which increases with Co content. For CoT20 the intensity of these two peaks does not change from 0.75 h to 168 h treatment (Fig. 6c). In contrast to the layered precursors, the Mn_χ for the reflux products increases over time (Fig. 7b), reaching an approximate plateau after 1 week, but the final dissolved ratio is also negatively correlated with the concentration of Co in the samples. Akin to the

layered precursors, this negative correlation might indicate that as Co content increases less Mn is sorbed and thus less Mn is readily removed during the acid treatment. The Co_χ values for the reflux products (Fig. 7d) are similar to those of the layered precursors in that they systematically increase with time, but again, Co_χ values are low suggesting that Co is largely structurally incorporated in the reflux products. Finally, the fast and complete release of Mg to solution (Fig. 7e) indicates that all Mg is present as exchangeable and/or sorbed cations in the reflux products. As XRD shows the sole presence of $\sim$9.6 Å Mn oxides in the untreated reflux products, the additional presence of $\sim$7.2 Å layered minerals after acid treatment indicates that at least part of the released Mg was originally located in phyllomanganate interlayers, its release leading to the observed shift of the layer-to-layer distance from $\sim$9.6 Å to $\sim$7.2 Å. Taken together, the release of Mg to solution upon acid treatment and the presence of characteristic reflections of birnessite in acid-treated CoT10, CoT15 and CoT20 indicate that CoT10, CoT15 and CoT20 contain a mixture of both layered and tunnel structures, consistent with XRD and FTIR data.

3.2. Morphology of the reflux products

All reflux products consist of platelets and fibers as shown in HRTEM images (Fig. 8). As expected, Tod occurs mostly as fibrous laths aligned with each other at 120° to form large aggregates with a network-like morphology (Fig. 8a, b and c). Both fibrous and trilling patterns are characteristic growth morphologies of todorokite and have been reported in both synthetic and natural samples (e.g., Siegel and Turner, 1983; Golden et al., 1986; Feng et al., 2004; Bodeï et al., 2007; Atkins et al., 2014). Overall the Tod fibers (Fig. 8c) exhibit lattice fringes with fringe widths of $\sim$1 nm, which corresponds to 3 [MnO$_6$] octahedra, representing the 3×3 tunnel size of ideal todorokite. In the network-like plates (Fig. 8b) however, there are incoherent tunnel intergrowths with dimensions of 3×4, 3×5, 3×7, 3×8, 3×10 and 3×12 [MnO$_6$] octahedra, as reported by Feng et al. (1999), indicating that in the trilling intergrowths the tunnel size in the a^* direction is variable. The observation of these non-ideal $3 \times n$ tunnel structures is consistent with the XRD for Tod. The images of the Co-containing reflux products are similar to those of Tod, but CoT samples contain fewer fibers (Fig. 8i and j) and more plates (Fig. 8d–h). In addition, two kinds of plates, with and without lattice fringes, can be distinguished in the CoT samples. In the plates with lattice fringes there does not appear to be a predominant fringe size. Representative images are shown for CoT5 and CoT20 in Fig. 8e, k and l, with fringe widths corresponding to 3, 4, 5, 6, 7, 9, 10, 11, 12 and 13 [MnO$_6$] octahedra, corresponding to a wide range of $3 \times n$ ($n \geq 3$) tunnel sizes. The increased abundance of non-ideal $3 \times n$ tunnel sizes, compared to Tod, agrees with the XRD for the CoT samples. Plates with smooth surfaces and without visible lattice fringes are observed in CoT20 (Fig. 8j), both features being characteristic of layered structures. The presence of layered structures in the reflux products is consistent with the XRD,

$$y = \frac{C_t}{C}$$

c_t: detected concentration of Mn, Co or Mg at different time intervals;

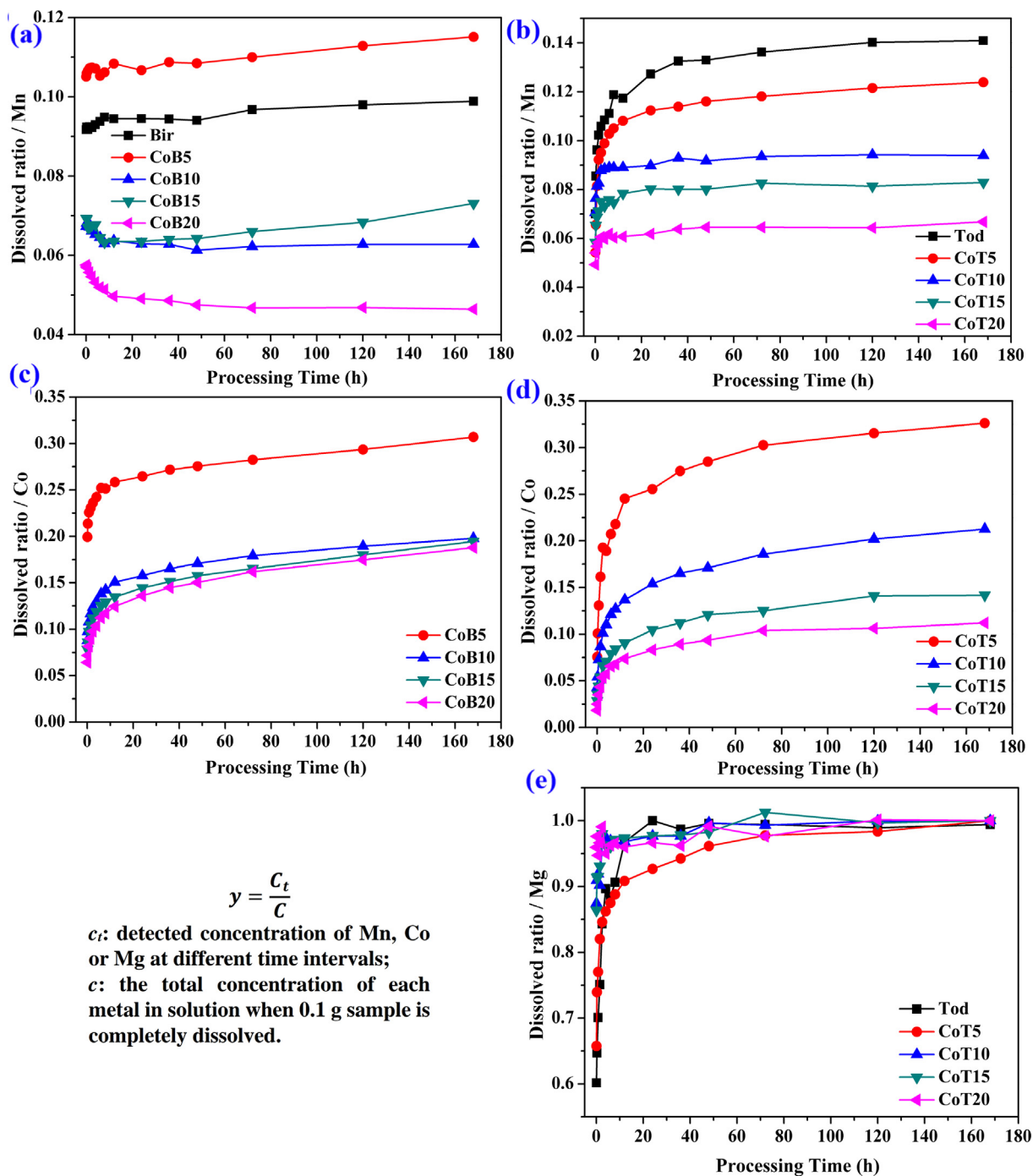c: the total concentration of each metal in solution when 0.1 g sample is completely dissolved.

Fig. 7. Ratios of element (Mn, Co, Mg) released during nitric acid treatment. Mn for CoB (a) and CoT (b). Co for CoB (c) and CoT (d). Mg for CoT (e).

FTIR and acid treatment results. Electron diffraction patterns of representative plates for Tod, CoT5, CoT15 and CoT20 (Supplementary Information Fig. S3) are all similar, and show pseudo-hexagonal symmetry due to the fringes arranged in three directions (Golden et al., 1986). The presence of Co in these plates is supported by the energy dispersive spectrometry peak at ∼6900 eV (Co Kα) (Supplementary Information Fig. S3).

3.3. Physicochemical analyses of layered precursors and reflux products

The elemental composition of the layered precursors and reflux products (Table 4) indicate that as Co content increases in the CoB and CoT samples the Mn content decreases significantly, relative to Bir and Tod, respectively. This is likely due to the substitution of Co for Mn in the

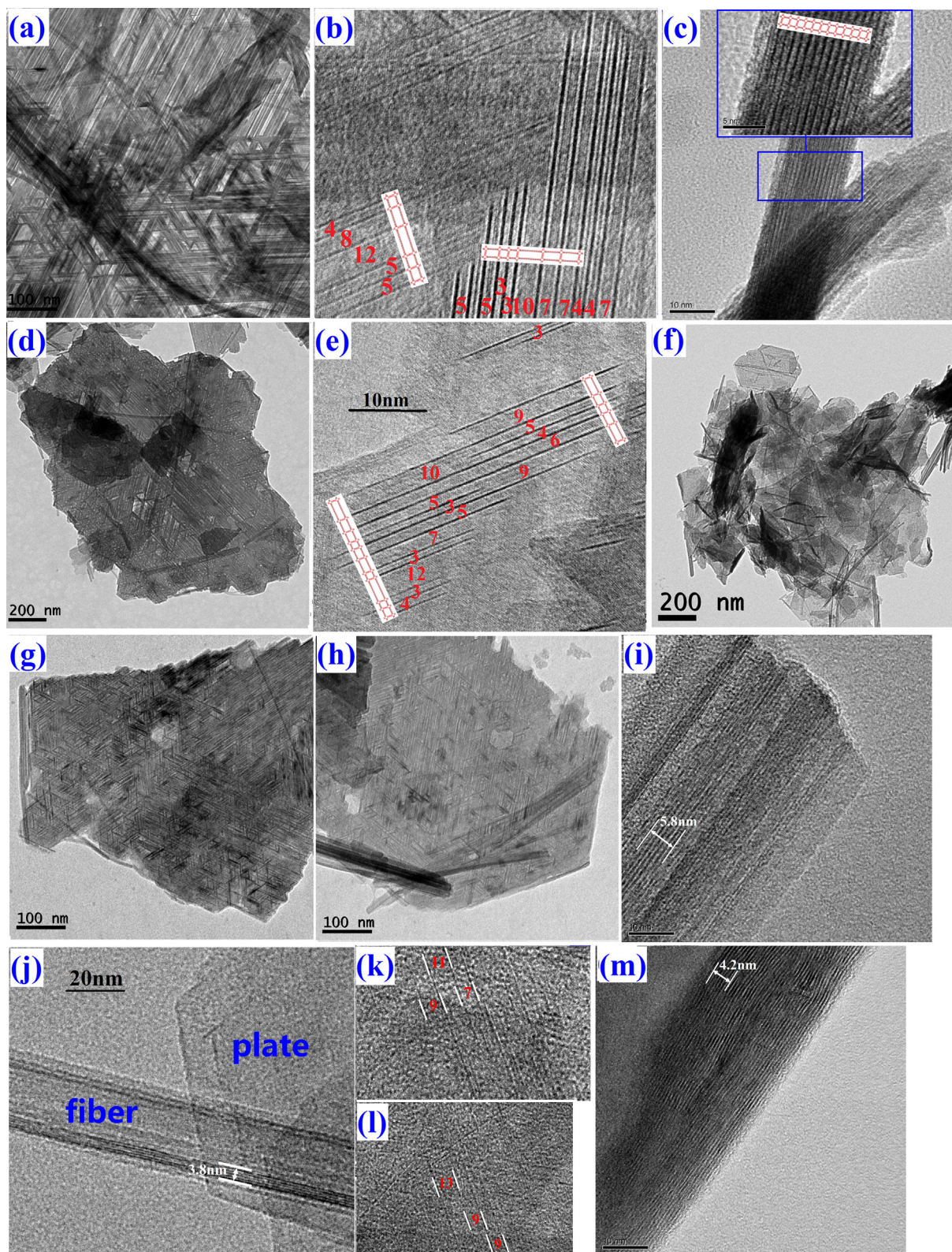Fig. 8. High resolution transmission electron microscopy images: Tod: (a-c); CoT5: (d and e); CoT10: (f); CoT15: (g); CoT20: (h-m). Red numbers in the pictures indicate the number of MnO$_6$ octahedra between lattice fringes, models schematize the structure of marked areas observed along the b^* direction. White labels in (i), (j) and (m) indicate the distance corresponding to 6, 4 and 6 lattice fringes, respectively.

crystal structure (Loganathan and Burau, 1973; Onda et al., 2007), although there is likely some surface adsorption of Co at the edge sites and/or above and below the vacancy sites (Manceau et al., 1997). It is noticeable that the Mn content in the reflux products shows a greater reduction than in the corresponding layered precursors, with no significant modification of the average oxidation state (AOS) of Mn (Table 3). On the other hand, the Co content (wt% and mol%) is approximately equivalent or slightly higher in the reflux products compared to their corresponding layered precursors. This may indicate that during reflux more Mn is lost from the layered precursors relative to Co and that the transformation of the layered precursors into tunnel products favours the structural incorporation of Co.

The surface areas of CoT samples are significantly lower than that of Tod (Table 4), which might indicate that the todorokite-like product in the CoT samples (or the mixture of the todorokite-like product and layered Mn oxides) has increased particle size compared to Co-free Tod.

The conductivity of the reflux solutions measured at the end of the reflux process are 26.4, 23.5, 32.0, 25.6 and 24.8 µS/cm for Tod, CoT5, CoT10, CoT15 and CoT20, respectively, indicating that the release to solution of Co, Mn and Mg and corresponding OH and residual Cl anions during

todorokite formation was limited. The total concentration of dissolved solids derived from the conductivity values (McNeil and Cox, 2000) is ~20 mg/L, equating to a dissolution of ~8 mg of solid from the initial 5–7 g used in each reflux.

3.4. Crystal chemistry of Mn and Co in layered precursors and reflux products

3.4.1. Mn K-edge XANES

The Combo method (Manceau et al., 2012) is applied to fit the first derivatives of the Mn K-edge XANES spectra to determine the proportions of Mn(II), Mn(III) and Mn(IV), and thus the Mn AOS in the layered precursor and reflux minerals. Results are shown in Table 3 and the Supplementary Information (Fig. S4 and Table S1). The CoB and CoT samples possess more Mn(IV) and less Mn(III) relative to Bir and Tod, respectively, slightly increasing the Mn AOS, consistent with previous reports (Manceau et al., 1997). The decrease in Mn(III) relative to Bir and Tod most likely arises from Co(III) substitution for Mn(III) (Manceau et al., 1997; Song et al., 2010; Simanova and Peña, 2015). The Mn AOS values are not significantly different between the layered precursors and their reflux products, however, consistent with previous work (Atkins et al., 2014).

3.4.2. Mn K-edge EXAFS

In Mn K-edge EXAFS spectra, the region from $6.5 \sim 9.5$ $Å^{-1}$ is especially sensitive to the crystal chemistry of Mn in the Mn oxide structure (McKeown and Post, 2001; Manceau et al., 2002, 2004; Gaillot et al., 2003) and as such it is defined as an "indicator" region for Mn oxides (Marcus et al., 2004; Manceau et al., 2004). The frequency, amplitude and shape of the Mn K-edge EXAFS spectra are similar over the entire wavenumber range for all samples, indicating that they possess a common basic structure (Grangeon et al., 2010; Fig. 9a and b). Notably however, the frequencies of the CoB and CoT spectra are right-shifted relative to Bir and Tod spectra, respectively (Fig. 9a and b). In agreement with the Mn AOS results, this is attributed to a decrease in Mn(III) content (Marcus et al., 2004) and the associated reduction of interatomic distances. Furthermore, the amplitude and shape of the spectra for

Table 3
Fractional and average valence states of Mn obtained from a Combo fit of Mn K-edge XANES 1st derivative spectra of layered precursors and reflux products. The estimated error for Combo method is ±4% (Manceau et al., 2012; Yin et al., 2015).

Sample	Mn^{2+} at. %	Mn^{3+} at. %	Mn^{4+} at. %	Mn-AOS
Bir	2	26	72	3.69
CoB5	3	17	81	3.78
CoB10	4	27	69	3.64
CoB15	5	7	88	3.83
CoB20	5	9	86	3.80
Tod	2	25	74	3.72
CoT5	2	23	75	3.73
CoT10	4	26	70	3.66
CoT15	2	16	82	3.81
CoT20	5	8	87	3.82

Note: The references used to fit Mn K-edge XANES data are those used by Manceau et al. (2012).

Table 4
Physicochemical properties of layered precursors and reflux products.

Samples	Mn wt%	Mg wt%	Mg/Mn mol%	Mg/(Mn + Co) mol%	SSA (m²/g)
Bir	55.4(1.0)	–	–	–	–
CoB5	54.0(2.0)	–	–	–	–
CoB10	52.3(2.3)	–	–	–	–
CoB15	49.2(7)	–	–	–	–
CoB20	45.0(1.8)	–	–	–	–
Tod	54.4(2.1)	3.95(8)	16.4	16.4	90.7
CoT5	48.0(1.2)	3.86(9)	18.2	16.9	47.6
CoT10	46.0(1.5)	3.67(12)	18.1	17.5	86.2
CoT15	40.9(1.2)	3.72(2)	20.6	16.6	51.1
CoT20	39.6(7)	3.58(7)	20.4	17.0	55.0

Note: Na was not detected in samples prepared by Song et al. (2010) with the same method and thus not measured in the present samples.
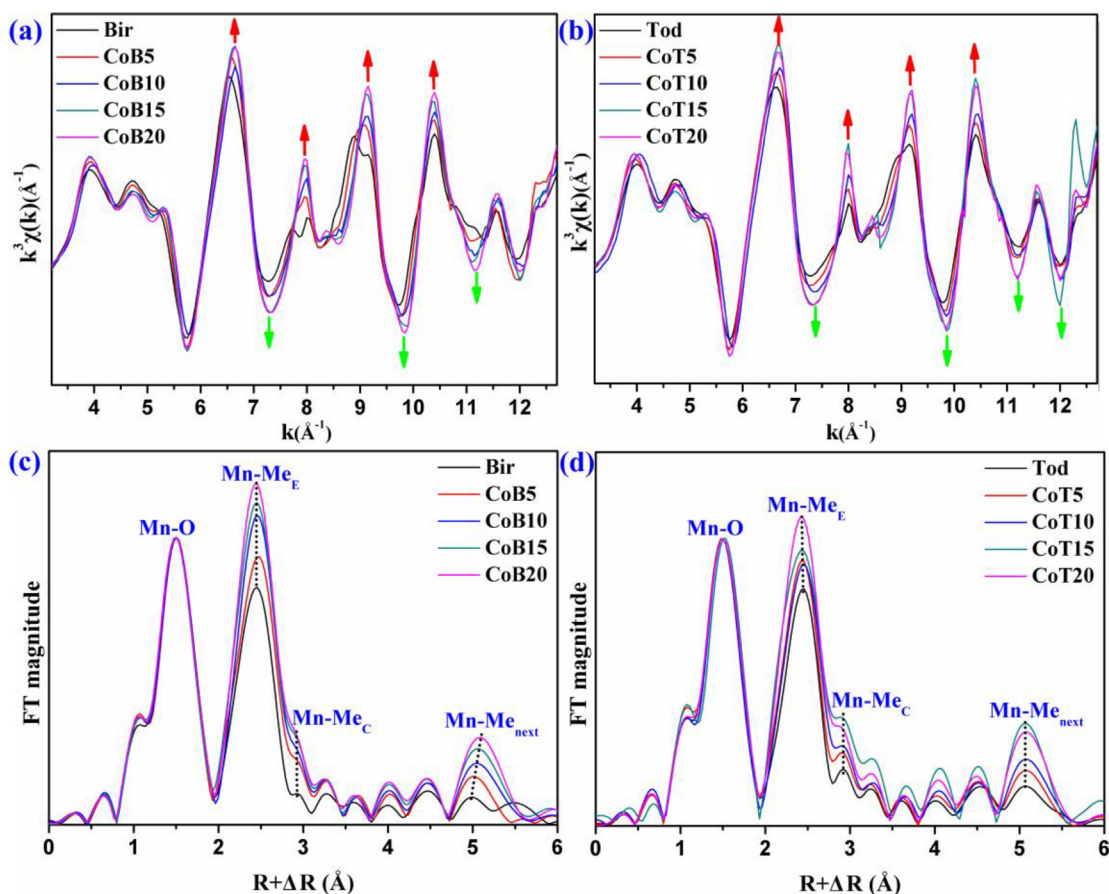
Fig. 9. Mn K-edge EXAFS spectra (a and b) and their respective Fourier transforms (c and d) for layered precursors and reflux products. Arrows in (a) and (b) highlight modifications of signal amplitude (see text for details). Intensity of the Fourier transforms are normalized to the first Mn-O shell (c and d).

the layered precursors and reflux products evolve as a function of Co content (Fig. 9a and b). Specifically, with increasing Co content the features at 6.8, 8.0, 9.3 and 10.5 $Å^{-1}$ and the troughs at 7.3, 9.8 and 11.2 $Å^{-1}$ increase in amplitude and become sharper. In particular, for Bir, the features at ~8 and ~9 $Å^{-1}$ have relatively low amplitude and are split, as expected for triclinic birnessite, reflecting the pseudo-orthogonal layer symmetry in its sheets (Manceau et al., 2004; Webb et al., 2005; Gaillot et al., 2007). With increasing Co content, these features increase in amplitude and become single peaks, as expected for hexagonal birnessite, and consistent with a lower content of Jahn-Teller distorted octahedra in the layer structure (Manceau et al., 2004; Marcus et al., 2004; Gaillot et al., 2007). As such, both the XRD and Mn K-edge EXAFS indicate that the layered precursors evolve from triclinic birnessite (Bir) to hexagonal birnessite (CoB15, CoB20) with increasing Co content. For Tod, the features at ~8 and ~9 $Å^{-1}$ have relatively low amplitude and the feature at ~9 $Å^{-1}$ is broad with a pronounced shoulder on the low wavenumber side, consistent with todorokite spectra (Webb et al., 2005; Feng et al., 2010; Atkins et al., 2014). With increasing Co content these features increase in amplitude and the feature at ~9 $Å^{-1}$ becomes much sharper with

a loss of the shoulder shape, resembling more closely the shape expected for layered Mn oxides (McKeown and Post, 2001; Webb et al., 2005). As such, the XRD, FTIR, acid treatment, HRTEM and Mn K-edge EXAFS all indicate that the reflux products contain a mixture of layered and tunnel Mn oxides.

Concomitant changes are evident in the Fourier transforms of the CoB and CoT spectra, relative to the Bir and Tod spectra, respectively (Fig. 9c and d). The three peaks at ~1.5, ~2.5 and ~3 Å (R+ΔR) are common to layered and tunnel structure Mn oxides and correspond to the first Mn-O, first Mn-Me edge-sharing (Mn-Me$_E$) and second Mn-Me corner-sharing (Mn-Me$_C$) shell distances, respectively (e.g., Manceau et al., 1988, 2007; Silvester et al., 1997; Gaillot et al., 2003; Marcus et al., 2004; Peacock and Sherman, 2007b; Peña et al., 2010). The Mn-Me$_E$ distance reflects the interatomic distance between adjacent edge-sharing Mn-Mn octahedra, present in the layers of layered Mn oxides, and in the walls and ceilings of tunnel Mn oxides (Fig. 1). The Mn-Me$_C$ distance reflects the interatomic distance between adjacent corner-sharing Mn-Mn octahedra, which can be present in both layered and tunnel Mn oxides when cations adsorb above/below vacant layer sites and/or at edge sites (Manceau et al., 2007), but are lar-

gely present in tunnel Mn oxides due to the configuration of the Mn2 / Mn4 sites (Fig. 1) (Kim et al., 2003; Webb et al., 2005). Notably, the reflux products show a more defined and thus easily identifiable peak at ~3 Å (R+ΔR) compared to their corresponding layered precursor, but the definition of this feature weakens with increasing Co content. This suggests that the reflux products contain more corner-sharing linkages than their layered precursors, but that the proportion of these linkages, and thus the proportion of todorokite-like structures in the reflux products, decreases with increasing Co content, consistent with FTIR results.

To interpret the Mn K-edge EXAFS more quantitatively, the spectra were fit using a procedure similar to that of Grangeon et al. (2010). Fit parameters are shown in Table 5 and the Supplementary Information (Fig. S5). The fitting results show that the Mn-Me_E bond distances of the layered precursors and reflux products steadily decrease with increasing Co content (Table 5 and Fig. 10). This is likely caused by the substitution of smaller Co(III) for Mn(III), as also evidenced by the shift towards lower d-values of the high-angle XRD peaks for the CoB and CoT samples (Fig. 2). Results also show that the ratio of Mn-Me_C to Mn-Me_E (CN_C/CN_E) increases from the CoB to CoT samples, and decreases slightly from Co-free Tod to Co-containing CoT20, confirming that the reflux products contain more corner-sharing linkages than their layered precursors, and supporting the inference that the proportion of corner-sharing linkages in the reflux products, and thus of todorokite-like structures, decreases with increasing Co content (Table 5).

The Mn K-edge χ(k) spectra were also fit as a linear combination of the CoT5 and corresponding CoB spectra, used as reference compounds for tunnel and layered Mn oxides, respectively, to assess the relative proportions of both components in the reflux products (Table 6 and the Supplementary Information, Fig. S6). Fitting indicates that CoT10, CoT15 and CoT20 contain ~80–70% layered ~9.6 Å Mn oxide and ~20–30% tunnel todorokite-like Mn oxide. These values are in good agreement with the proportions of layered and tunnel Mn oxides in natural hydrothermal ferromanganese samples (Atkins et al., 2016). The linear combination fitting results indicate that the proportion of todorokite-like structures in the reflux products decreases with increasing Co content, consistent with the FTIR results and the Mn K-edge EXAFS fitting.

3.4.3. Co K-edge EXAFS

The frequency, amplitude and shape of the Co K-edge EXAFS spectra, in both k- and r-space, are very similar to one another for both the layered precursors (except for CoB5 which has low Co content and is therefore poor quality) (Fig. 11a) and the reflux products (Fig. 11b). These spectra resemble those collected at the Mn K-edge EXAFS, thus implying that Co possesses a very similar local coordination environment in the layered and reflux samples, and that this environment is similar to that of Mn.

To interpret the Co K-edge EXAFS more quantitatively, spectra are fit using a procedure similar to that of Grangeon et al. (2010). Fit parameters are shown in Table 7 and the Supplementary Information (Fig. S7). In this fitting

Table 5
Structural parameters derived from Mn K-edge EXAFS fitting over 1–4 Å.

Atomic pairs		Bir	CoB5	CoB10	CoB15	CoB20	Tod	CoT5	CoT10	CoT15	CoT20
Mn-O_1st	CN	5.36(89)	5.04(59)	4.30(51)	5.35(64)	5.15(62)	5.46(66)	5.57(69)	4.97(51)	5.51(1.05)	5.44(72)
	R (Å)	1.907(7)	1.908(5)	1.909(5)	1.904(5)	1.906(5)	1.901(6)	1.901(5)	1.903(4)	1.904(8)	1.903(5)
	σ² (Å²)	0.004(1)	0.003(1)	0.003(1)	0.004(1)	0.004(1)	0.004(1)	0.004(1)	0.003(1)	0.004(1)	0.004(1)
Mn-O_2nd	R (Å)[a]	3.610(81)	3.656(31)	3.641(33)	3.644(31)	3.635(30)	3.582(57)	3.601(40)	3.625(29)	3.636(78)	3.623(34)
Mn-Me_E	CN	5.91(1.54)	6.19(75)	5.00(67)	6.12(68)	5.58(68)	4.63(90)	5.22(76)	4.99(59)	5.49(93)	5.53(75)
	R (Å)	2.901(10)	2.895(6)	2.884(6)	2.874(6)	2.871(7)	2.883(7)	2.874(6)	2.874(6)	2.866(8)	2.864(6)
	σ² (Å²)	0.008(2)	0.007(1)	0.005(1)	0.006(1)	0.005(1)	0.006(1)	0.006(1)	0.006(1)	0.005(1)	0.005(1)
Mn-Me_C	CN	2.61(1.32)	2.76(71)	2.14(55)	2.69(65)	2.52(54)	2.60(83)	2.97(70)	2.75(58)	2.99(88)	2.86(76)
	R (Å)	3.466(72)	3.512(23)	3.501(24)	3.500(20)	3.496(18)	3.450(38)	3.463(23)	3.483(18)	3.485(37)	3.477(18)
CN_C/CN_E		0.44	0.45	0.43	0.44	0.45	0.56	0.57	0.55	0.54	0.52
δE_0 (eV)		−7.12(1.63)	−6.56(1.04)	−5.49(98)	−8.17(1.12)	−7.38(98)	−7.15(1.33)	−8.12(1.07)	−5.35(95)	−7.98(1.66)	−8.14(1.05)
R factor (%)		0.04	0.01	0.01	0.01	0.01	0.02	0.02	0.01	0.01	0.01

Coordination numbers (CN) and Debye-Waller factors (σ²) of Mn-O shells were refined together, as were Debye-Waller factors of the two Mn-Me shells.
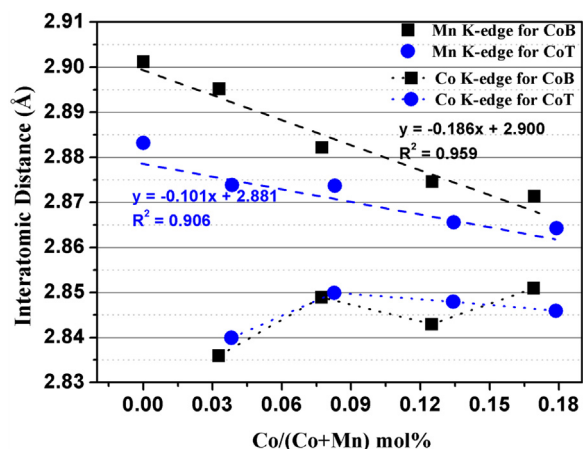
Fig. 10. Evolution of interatomic Mn/Co-Me$_E$ distances in layered precursors and reflux products as a function of their Co content.

Table 6
Best fits via linear combination fitting of Mn K-edge $\chi(k)$ for reflux products.

Sample	Best fitting	Error
CoT10	0.33 CoT5 + 0.67 CoB10	0.09
CoT15	0.23 CoT5 + 0.77 CoB15	0.07
CoT20	0.21 CoT5 + 0.79 CoB20	0.04

approach, a f parameter is used to estimate the relative proportion of Co in Co-Me$_E$ edge-sharing configuration in the CoB and CoT samples (Table 7). Similar to the Mn K-edge spectra, the Co-Me$_E$ edge-sharing peak reflects the interatomic distance between adjacent edge-sharing Co-Me octahedra, and can result from the incorporation of Co into the layers of layered Mn oxides (where Co should be surrounded by 6 edge-sharing Mn), and the incorporation of Co into the walls or ceilings of tunnel Mn oxides (where Co at the Mn1/Mn3 site should be surrounded by 6 edge-sharing Mn, while Co at the Mn2/Mn4 site should be surrounded by 4 edge-sharing Mn) (Fig. 1). As such the relative proportion of Co in Co-Me$_E$ edge-sharing configuration represents the total proportion of Co that is structurally incorporated in the layered precursors and combined layered and tunnel structure reflux products. The Co-Me$_C$ corner-sharing peak reflects the interatomic distance between corner-sharing Co-Me octahedra, and can result from the surface adsorption of Co at triple corner and/or edge sites on layered and tunnel Mn oxides, and from the incorporation of Co into the walls or ceilings of tunnel Mn oxides (at the Mn2/Mn4 site where Co should be surrounded by 4 corner-sharing Mn) (Fig. 1). For all samples, data was fit assuming that the coordination number of Co in Co-Me$_E$ edge-sharing configuration is 6. This might lead to an overestimation of Co in Co-Me$_E$ edge-sharing configuration, and thus of Co that is structurally incorporated in the CoT samples, because Co incorporated into tunnel structures might occupy the Mn2/Mn4 site with a Co-Me$_E$ edge-sharing coordination number of 4 (Song et al., 2010). In this case the Co-Me$_E$ edge-sharing coordination number for the CoT samples would be slightly less

than 6, and equate to the weighted average of the proportion of Co at the Mn1/Mn3 site, surrounded by 6 edge-sharing Mn, and Co at the Mn2/Mn4 site, surrounded by 4 edge-sharing Mn. Despite this limitation, the approach provides a reasonable estimate of the ratio of Co in Co-Me$_E$ edge-sharing configuration and thus the proportion of Co that is structurally incorporated in the layered precursors and the combined layered and tunnel structure reflux products.

Fitting results show that Co-Me$_E$ bond distances of the layered precursors and reflux products do not significantly change with increasing Co content (Table 7 and Fig. 10), indicating that Co incorporated into the precursor and reflux products is uniformly distributed in the crystals, being mainly surrounded by Mn(IV). Results also show that the f parameter, and thus the proportion of nominally structurally incorporated Co, is almost equivalent for the CoB and CoT samples at ~80% (Table 7). For the CoB samples, the distribution of Co between incorporated (~80%) and surface adsorbed (~20%) species is consistent with previous reports (Manceau et al., 1997; Kwon et al., 2013; Yin et al., 2013, 2015). For the CoT samples, which contain a mixture of layered (~80–70%) and tunnel (~20–30%) structure Mn oxides, the distribution of Co between incorporated (~80%) and surface (~20%) species reflects the average coordination environment. Given the limitations of the fitting approach, the proportion of the total Co incorporated into the CoT samples might be less than ~80%.

4. DISCUSSION

4.1. Effect of Co on the transformation of birnessite to todorokite

Layered birnessite precursors with a range of Co contents from 0 to 20 Co/(Mn + Co) mol% were subjected to a reflux process designed to simulate the transformation of birnessite into todorokite in natural environments. Of the total Co sorbed in the layered birnessite precursors, ~80% is structurally incorporated and ~20% is surface adsorbed. Mineralogical data derived from XRD, FTIR, and acid treatment, combined with morphological data from HRTEM and molecular level data from Mn K-edge EXAFS indicate that, for the Co-free birnessite precursor, the reflux procedure produces a todorokite-like product with dominant ideal 3×3 tunnel sizes in fibrous laths and non-ideal $3 \times n$ ($n \geq 3$) tunnel sizes in trillings. In contrast, for the Co-containing birnessite precursors, the reflux procedure leads to todorokite-like products with a wide range of non-ideal $3 \times n$ ($n \geq 3$) tunnel sizes, with no apparent predominant tunnel dimension. Furthermore, for the Co-containing birnessite precursors, the reflux procedure yields Mn oxides with both ~9.6 Å layered structure and todorokite-like tunnel structure, in which the proportion of tunnel structures decreases with increasing precursor Co content. These results indicate that the presence of Co in birnessite disrupts its transformation to todorokite.

The ability of Co to disrupt the transformation of birnessite into todorokite and produce a non-ideal
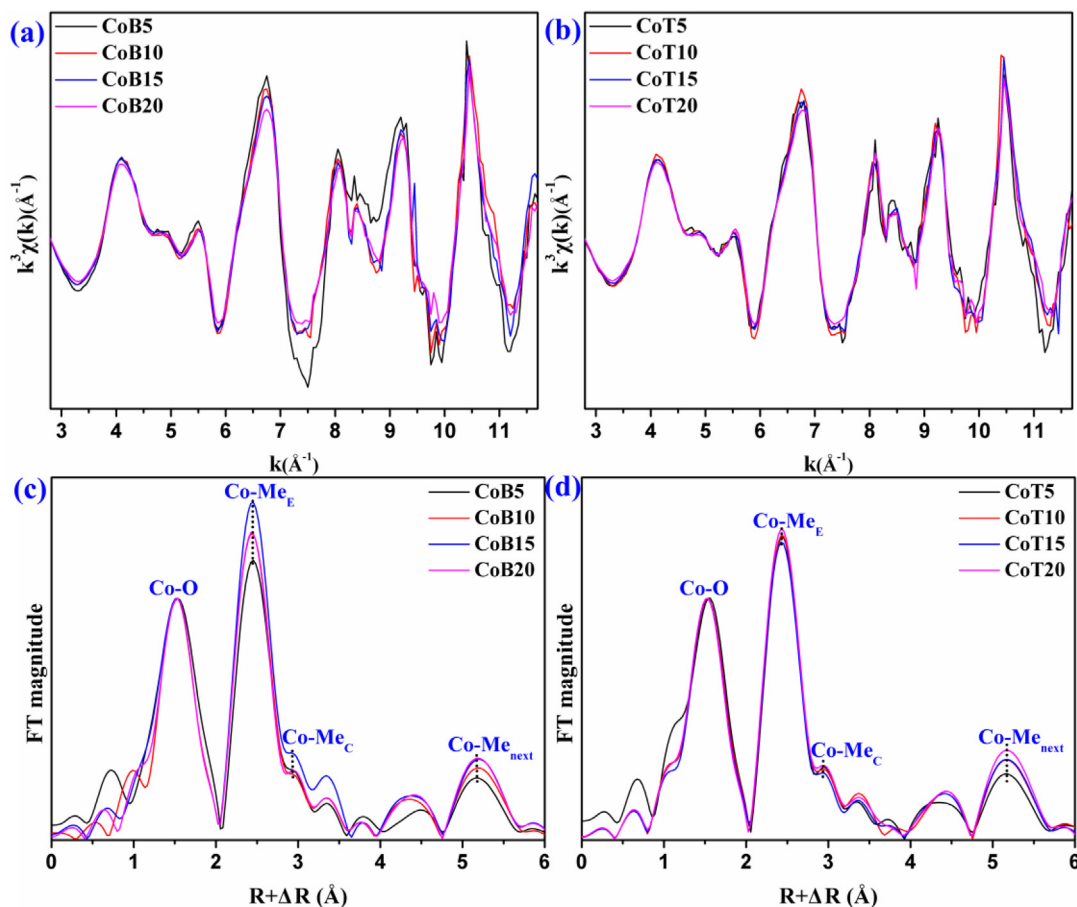
Fig. 11. Co K-edge EXAFS spectra (a and b) and their respective Fourier transforms (c and d) for layered precursors and reflux products. Intensity of the Fourier transforms are normalized to the first Mn-O shell (c and d).

Table 7
Structural parameters derived from Co K-edge EXAFS fitting over 1–4 Å.

Atomic pairs		CoB5	CoB10	CoB15	CoB20	CoT5	CoT10	CoT15	CoT20
Co-O1st	CN	6.62(1.58)	4.66(66)	5.75(88)	4.61(51)	7.21(2.62)	5.21(66)	4.91(59)	4.77(69)
	R (Å)	1.909(9)	1.913(5)	1.909(8)	1.915(5)	1.907(17)	1.913(6)	1.913(5)	1.914(7)
	σ^2(Å²)	0.001(1)	0.001(1)	0.004(1)	0.002(1)	0.004(2)	0.002(1)	0.002(1)	0.002(1)
Co-O2nd	R(Å)a	3.713(52)	3.460(46)	3.660(29)	3.495(35)	3.666(34)	3.469(45)	3.486(37)	3.481(44)
Co-MeE	CN	6*f	6*f	6*f	6*f	6*f	6*f	6*f	6*f
	R (Å)	2.836(14)	2.849(5)	2.843(6)	2.851(5)	2.840(13)	2.850(5)	2.848(5)	2.846(6)
	σ^2(Å²)	0.002(1)	0.003(1)	0.002(0.5)	0.003(0.5)	0.002(1)	0.003(1)	0.003(1)	0.003(1)
Co-MeC	CN	6*(1-f)	6*(1-f)	6*(1-f)	6*(1-f)	6*(1-f)	6*(1-f)	6*(1-f)	6*(1-f)
	R (Å)	3.528(68)	3.364(57)	3.474(16)	3.401(35)	3.475(34)	3.469(37)	3.395(29)	3.404(30)
f		0.84(13)	0.86(9)	0.75(5)	0.77(6)	0.73(14)	0.83(10)	0.79(7)	0.81(10)
$\delta E0$ (eV)		−3.75(2.50)	−0.81(91)	−2.09(1.32)	−0.37(94)	−3.13(2.62)	0.12(1.03)	−0.51(99)	−0.05(1.07)
R factor (%)		0.04	0.003	0.006	0.003	0.05	0.005	0.004	0.006

Coordination numbers (CN) and Debye-Waller factors (σ^2) of Co-O shells were refined together, as were Debye-Waller factors of the two Co-Me shells. Parameter f represents the proportion of Co in an edge-sharing configuration in each of the CoB and CoT sample.

todorokite-like product is very similar to that of Ni and can be attributed to the fact that both Ni(II) and Co(III) are not Jahn–Teller distorted cations. The presence of Jahn–Teller distorted Mn(III) in the birnessite layers is critical to the transformation of birnessite into todorokite because distortion of the Mn(III) octahedral due to the Jahn-Teller effect

results in an elongation and thus weakening of the Mn(III)–O bonds (Bodeï et al., 2007; Cui et al., 2008; Atkins et al., 2014; Grangeon et al., 2014, 2015; Zhao et al., 2015). It is at this structurally weak point that phyllomanganate layers are most susceptible to kinking which leads to the formation of the todorokite tunnel walls within the phylloman-

ganate interlayers (Atkins et al., 2014; Grangeon et al. 2014). Isomorphic substitution of Jahn–Teller distorted Mn(III) by Co(III) therefore reduces the likelihood of todorokite formation (Atkins et al., 2014, 2016). It is possible that the isomorphic substitution of Mn(III) by Co(III) results in an uneven distribution of Mn(III) within the layers (Grangeon et al., 2015). This might explain the fact that even the most Co-enriched birnessite precursors are able to form a significant proportion of tunnel structures, but that these tunnel structures have non-ideal tunnel dimensions $3 \times n$ ($n >> 3$ – CoT15 and CoT20, with n up to 13). It is noteworthy that ideal 3×3 tunnel structures are visible in the fibrous laths of the Co-free todorokite reflux product, whereas non-ideal $3 \times n$ ($n >> 3$) tunnel structures dominate in trilling intergrowths of the Co-containing todorokite-like reflux products. Other studies have also noted the predominance of ideal 3×3 tunnel dimensions in fibrous todorokite (Golden et al., 1986; Post et al., 2003; Feng et al., 2004; Cui et al., 2009). This suggests that ideal todorokite tends to exhibit a fibrous morphology while non-ideal or $\boldsymbol{a}$-disordered todorokite prefers to form trilling intergrowths, and that the presence of Co(III), and likely of other structurally incorporated non Jahn-Teller distorted cations, promotes the formation of a network-like platy morphology over a fibrous one.

In addition to the ability of Co(III) to disrupt the transformation of birnessite into todorokite, the interlayer species in the precursor layered phase may also be important for transformation. In this work a ~9.6 Å layered precursor with interlayer Mg was synthesized, and the acid treatment indicates that the reflux products with layered structures also contain Mg as the interlayer species. In the layered precursors, Mg is likely present in a hydrated form as $Mg(H_2O)_6^{2+}$, as for buserite (Shen et al., 1994; Post et al., 2003), but under reflux treatment these species might convert to a Mg (hydr)oxide, leading to an asbolane-like structure with islands of (hydr)oxides in the interlayer (Chukhrov et al., 1982, 1987; Manceau et al., 1987, 1992). Interestingly, although the acid treatment results in the dissolution of Mg and the collapse of the reflux product interlayers from ~9.6 to ~7.2 Å, it cannot distinguish between $Mg(H_2O)_6^{2+}$ and Mg (hydr)oxides as both are expected to dissolve and/or to be exchanged under acidic conditions. XRD patterns of reflux products prepared as in the present study and heat treated at 120 °C for 12 h do not show a ~7.2 Å peak (Song et al., 2010), however, as would be expected from the dehydration of $Mg(H_2O)_6^{2+}$ interlayer species (Chukhrov et al., 1987; Shen et al., 1994). The interlayer Mg species in the layered reflux products is therefore resistant to thermal dehydration and thus most likely resembles a (hydr)oxide-like species, similar to the islands of Co/Ni (hydr)oxides present in the interlayers of asbolane (Chukhrov et al., 1982, 1987; Manceau et al., 1987, 1992). The formation of Mg (hydr)oxides sandwiched between phyllomanganate layers should result in a slightly higher d-spacing for the layered reflux product compared to todorokite, and thus might explain the shift to higher d-values of the low-angle 00l peaks in the XRD patterns of the reflux products (Fig. 3c). Overall, we suggest that the formation of Mg (hydr)oxides during the reflux procedure results in

a mixture of stabilized ~9.6 Å asbolane-like layered structures and non-ideal todorokite-like tunnel structures in the reflux products.

The fact that Co(III), and other non Jahn–Teller distorted cations, structurally incorporated into birnessite disrupts the transformation of birnessite into todorokite might help explain the often observed predominance of phyllomanganates over tectomanganates in terrestrial and marine environments (e.g., Post, 1999; Marcus et al., 2004; Bodeï et al., 2007; Manceau et al., 2014), and the persistence of phyllomanganates in marine ferromanganese nodules and crusts that are many millions of years old (e.g., Burns and Burns, 1977).

4.2. Implications for the mobility and fate of Co during the transformation of birnessite to todorokite

To date only a limited number of studies have investigated the transformation of Co-containing layered Mn oxides into tunnel Mn oxides and the results indicate that precursor Co might be structurally incorporated into newly formed todorokite, by replacing Mn (Ching et al., 1999; Kumagai et al., 2005; Onda et al., 2007; Song et al., 2010). In particular, Song et al. (2010) hypothesize that Co primarily substitutes for Mn(III) in Co-containing todorokite, and that these Mn(III) are likely located at the edge sites (Mn2 and Mn4, Fig. 1) of the ideal 3×3 tunnel structure. As such Co(III) might be primarily incorporated at these edge sites (Ostwald, 1986; Song et al., 2010). The mineralogical, morphological and molecular level data obtained in the present study indicate that Co(III) is structurally incorporated into a mixture of ~9.6 Å asbolane-like and todorokite-like reflux products. Specifically, the shifts in the XRD patterns observed for the Co-containing reflux products, and the HRTEM images showing an enhanced occurrence of non-ideal $3 \times n$, or $\boldsymbol{a}$-disordered, todorokite with larger n (n up to 13), compared to Co-free todorokite, are both consistent with the presence of Co(III) isomorphically substituted for Mn(III). It is noteworthy that, eventually, as n approaches ∞ these tunnel structures will essentially become layered ones. This evolution is accompanied by an increased occurrence of plate-like network morphologies at the expense of fibrous ones. Consistent with these observations, the Co K-edge EXAFS data shows that Co(III) is predominantly present as a structurally incorporated species (~80%) in the mixed layered and tunnel Mn oxide reflux products. The EXAFS fitting procedure can to some extent differentiate between Co that is structurally incorporated at the Mn1/Mn3 sites vs. the Mn2/Mn4 sites of the newly formed tunnel structures (Fig. 1) because it provides an estimate of the ratio of Co in Co-Me$_E$ edge-sharing configuration compared to Co in Co-Me$_C$ corner-sharing configuration. The Co-Me$_E$ edge-sharing configuration includes Co incorporated into the layers of layered Mn oxides, effectively in a Mn1/Mn3 position, and Co incorporated into the walls or ceilings of tunnel Mn oxides, at both the Mn1/Mn3 site and the Mn2/Mn4 site. The Co-Me$_C$ corner-sharing configuration includes Co surface adsorbed at triple corner and/or edge sites on layered and tunnel Mn oxides, and Co incorporated into the walls or ceilings of tunnel Mn oxides at the Mn2/

Mn4 site. As such if there was a substantially different distribution of Co between the Co-Me$_E$ edge-sharing position in the precursors (i.e., Co incorporated in a Mn1/Mn3 position) and the Co-Me$_E$ edge-sharing positions in the reflux products (comprising the Mn1/Mn3 site and the Mn2/Mn4 site) then the estimate of the ratio of Co in Co-Me$_E$ edge-sharing configuration (i.e., the f parameter) should change. The fact that it does not is strong evidence that the Co coordination environment is at least largely similar between the precursors and the reflux products, and thus that the reflux products contain Co structurally incorporated at the Mn1/Mn3 non-edge sites. Previous reports suggest that Co might be incorporated at the Mn2/Mn4 edge sites and thus the precise location of structurally incorporated Co(III) in tunnel structure Mn oxides deserves further research.

The above evidence for structural incorporation of Co (III) in newly formed asbolane-like and todorokite-like Mn oxides can be combined with the physicochemical analyses to comment on the likely mobility of Co during the transformation process. The EXAFS data analysis shows that, from the Co-containing layered precursors to their corresponding reflux products, the distribution of Co between Co-Me$_E$ edge-sharing and Co-Me$_C$ corner-sharing configuration does not substantially change, and therefore the relative bulk distribution of Co is very similar. Moreover, the majority of the Co is present in Co-Me$_E$ edge-sharing configuration, and is thus structurally incorporated, with only a minor amount of Co present in Co-Me$_C$ corner-sharing configuration, either structurally incorporated in tunnel structures or surface adsorbed on layered and/or tunnel structures. For a given metal, structurally incorporated species are generally less susceptible to mobilisation than surface adsorbed species that can be desorbed due to fluctuations in environmental conditions (pH, ionic strength). The transformation process thus appears to maintain the strong sequestration of Co by Mn oxides. Furthermore, the conductivity measurements performed on the final reflux solutions indicate that the concentrations of ions in solution after the transformation process are low and thus the mass of Co lost to solution is also low.

Taken together these results suggest that Co(III) associated with layered birnessite precursors is retained in the solid phase during the transformation of birnessite/buserite to mixed ~9.6 Å asbolane-like and todorokite-like products. Despite the common ability of Ni(II) and Co(III) to disrupt the transformation of birnessite into todorokite, this result is in stark contrast to the mobility of Ni(II) during the transformation, where, with a similar proportion of structurally incorporated to surface adsorbed cation, ~50% of the Ni(II) initially associated with the birnessite precursor is released to solution during the transformation (Atkins et al., 2016). The difference in the mobility and fate of Ni(II) and Co(III) during the phyllomanganate-to-tectomanganate transformation may be attributed to the differences in their ionic radii and charge. Considering the ionic radii of Ni(II) (0.68 Å) and Co(III) (0.54 Å, low spin) compared to Mn(III) (0.58 Å, low spin), the steric match between Co(III) and Mn(III) is favorable over that between Ni(II) and Mn(III), and has been cited as a key parameter

for Co uptake by and structural incorporation in Mn oxides (Burns, 1976; Manceau et al., 1997). Considering the ionic charge, or electronegativity of Ni(II) and Co(III), Co(III) possesses a higher electronegativity than Ni(II) (1.791 vs. 1.574, respectively) and one that is much closer to that of Mn(III) (1.705, low spin) and Mn(IV) (1.923) (Yin et al., 2013), and thus its incorporation maintains better charge balance. Density functional theory modelling of Co(III) and Ni(II) uptake by birnessite shows that the energy difference between structural incorporation vs. surface adsorption as a triple corner-sharing complex is much lower for Co(III) compared to Ni(II) (Δ-value is -214 kJ/mol vs. –23 kJ/mol). Incorporation of Co(III) is therefore favoured over Ni(II) and moreover, this incorporation is favoured over surface adsorption (Kwon et al., 2013).

Overall the differences in the ionic properties of Co(III) and Ni(II) mean that, although both Ni(II) and Co(III) are non Jahn–Teller distorted, Co(III) provides a more favourable match to the layered and tunnel structure Mn (III) sites compared to Ni(II), and Co(III) is therefore incorporated in the mixed layered and newly formed tunnel structures. By comparison, ~50% of Ni(II) associated with precursor layer structures is lost to solution during the transformation and the remaining Ni(II) is only surface adsorbed on newly formed todorokite, meaning that it is susceptible to desorption and loss to solution (Atkins et al., 2016). More generally it is apparent that the mobility and fate of transition metals associated with Mn oxides depends on a number of metal properties, including Jahn–Teller distortion, ionic radius and electronegativity, where metal behaviour is selectively dictated by the structure of the Mn oxide. This means that Mn oxides with distinct structures (i.e. layered or tunnel structures) are likely to play unequal roles in the mobility and fate of transition metals in the environment.

5. SUMMARY AND CONCLUSIONS

The present study reports the first detailed investigation of the effect of Co content on the transformation of layered precursor Mn oxide birnessite into tunnel structure Mn oxide products, and documents the mobility and fate of Co during the transformation process. The structural incorporation of Co in layered birnessite precursors leads to an overall reduction of Jahn-Teller distorted Mn(III) octahedra in these precursors, a key factor for their transformation to tunnel structures. As a consequence, the presence of such structural Co(III) disrupts the transformation of birnessite into todorokite, leading to the coexistence of a ~9.6 Å asbolane-like phyllomanganate and a non-ideal, or *a*-disordered, todorokite-like tectomanganate. Non-ideal todorokite appears as trilling intergrowths with a wide range of tunnel dimensions that form a network plate-like morphology. Contrary to Ni(II), which also disrupts the transformation of layered to tunnel structures, Co(III) is retained in the solid transformation products, predominantly as structurally incorporated species. The results suggest that Co(III) is likely present in the Mn1 and Mn3 non-edge sites of todorokite, in contrast to previous reports. Overall, the transformation of Co-containing birnessite into todorokite in soils and sediments is unlikely to provide a

significant source of Co to soil and sediment porewaters. The present study compared to the results of previous work on the behaviour of other transition metals during the transformation of birnessite to todorokite demonstrates that, overall, metal mobility depends on a specific set of metal properties, the relative importance of these being likely dictated by the structure of the host Mn oxide.

ACKNOWLEDGEMENTS

APPENDIX A. SUPPLEMENTARY MATERIAL

Supplementary data to this article can be found online at https://doi.org/10.1016/j.gca.2018.11.001.

REFERENCES

Atkins A. L., Shaw S. and Peacock C. L. (2014) Nucleation and growth of todorokite from birnessite: implications for tracemetal cycling in marine sediments. *Geochim. Cosmochim. Acta* **144**, 109–125.

Atkins A. L., Shaw S. and Peacock C. L. (2016) Release of Ni from birnessite during transformation of birnessite to todorokite: Implications for Ni cycling in marine sediments. *Geochim. Cosmochim. Acta* **189**, 158–183.

Bodeï S., Manceau A., Geoffroy N., Baronnet A. and Buatier M. (2007) Formation of todorokite from vernadite in Ni-rich hemipelagic sediments. *Geochim. Cosmochim. Acta* **71**, 5698–5716.

Burns R. G. (1976) The uptake of cobalt into ferromanganese nodules, soils, and synthetic manganese (IV) oxides. *Geochim. Cosmochim. Acta* **40**(1), 95–102.

Burns R. G. and Burns V. M. (1975) Mechanism for nucleation and growth of manganese nodules. *Nature* **255**, 130–131.

Burns R. G. and Burns V. M. (1977) The mineralogy and crystal chemistry of deep-sea manganese nodules, a polymetallic resource of the twenty-first century. *Phil. Trans. R. Soc. London* **A286**, 283–301.

Burns R. G., Burns V. M. and Stockman H. W. (1983) A review of the todorokite-buserite problem; implications to the mineralogy of marine manganese nodules. *Am. Mineral.* **68**, 972–980.

Burns R. G., Burns V. M. and Stockman H. W. (1985) The todorokite-buserite problem: further considerations. *Am. Mineral.* **70**, 205–208.

Ching S., Krukowska K. S. and Suib S. L. (1999) A new synthetic route to todorokite-type manganese oxides. *Inorg. Chim. Acta* **294**, 123–132.

Chukhrov F. V., Drits V. A. and Gorshkov A. I. (1987) Structural transformations of manganese oxides in oceanic nodules. *Int. Geol. Rev.* **29**, 110–121.

Chukhrov F. V., Gorshkov A. I., Vitovskaya I. V., Drits V. A., Sistov A. V. and Rudnitskaya Y. S. (1982) Crystallochemical nature of Co-Ni asbolane. *Int. Geol. Rev.* **24**, 598–604.

Cui H., Feng X., Tan W., He J., Hu R. and Liu F. (2009) Synthesis of todorokite-type manganese oxide from Cu-buserite by controlling the pH at atmospheric pressure. *Micropor. Mesopor. Mat.* **117**, 41–47.

Cui H., Liu F., Feng X., Tan W. and Wang M. (2010) Aging promotes todorokite formation from layered manganese oxide at near-surface conditions. *J. Soil Sediment* **10**, 1540–1547.

Cui H., Liu X., Tan W., Feng X., Liu F. and Ruan H. D. (2008) Influence of Mn (III) availability on the phase transformation from layered buserite to tunnel-structured todorokite. *Clays Clay Miner.* **56**, 397–403.

Davies S. H. R. and Morgan J. J. (1989) Manganese (II) oxidation kinetics on metal oxide surfaces. *J. Colloid Interface Sci.* **129**, 63–77.

Drits V. A., Lanson B. and Gaillot A. C. (2007) Birnessite polytype systematics and identification by powder X-ray diffraction. *Am. Mineral.* **92**, 771–788.

Drits V. A., Silvester E., Gorshkov A. I. and Manceau A. (1997) Structure of synthetic monoclinic Na-rich birnessite and hexagonal birnessite: I. Results from X-ray diffraction and selected-area electron diffraction. *Am. Mineral.* **82**, 946–961.

Dublet G., Juillot F., Brest J., Noel V., Fritsch E., Proux O., Olivi L., Ploquin and Morin G. (2017) Vertical changes of the Co and Mn speciation along a lateritic regolith developed on peridotites (New Caledonia). *Geochim. Cosmochim. Acta.* **217**, 1–15.

Feng Q., Kanoh H. and Ooi K. (1999) Manganese oxide porous crystals. *J. Mater. Chem.* **9**, 319–333.

Feng X., Tan W., Liu F., Wang J. and Ruans H. (2004) Synthesis of todorokite at atmospheric pressure. *Chem. Mater.* **16**, 4330–4336.

Feng X., Zhu M., Ginder-Vogel M., Ni C., Parikh S. and Sparks D. (2010) Formation of nano-crystalline todorokite from biogenic Mn oxides. *Geochim. Cosmochim. Acta* **74**, 3232–3245.

Fuller C. C. and Harvey J. W. (2000) Reactive uptake of trace metals in the hyporheic zone of a mining-contaminated stream, Pinal Creek, Arizona. *Environ. Sci. Technol.* **34**, 1150–1155.

Gaillot A. C., Drits V. A., Manceau A. and Lanson B. (2007) Structure of the synthetic K-rich phyllomanganate birnessite obtained by high-temperature decomposition of KMnO₄: Substructures of K-rich birnessite from 1000°C experiment. *Micropor. Mesopor. Mat.* **98**, 267–282.

Gaillot A. C., Flot D., Drits V. A., Burghammer M., Manceau A. and Lanson B. (2003) Structure of synthetic K-rich birnessites obtained by high-temperature decomposition of KMnO₄. I. Two-layer polytype from a 800°C experiment. *Chem. Mater.* **15**, 4666–4678.

Golden D. C., Chen C. C. and Dixon J. B. (1986) Synthesis of todorokite. *Science* **231**, 717–719.

Grangeon S., Fernandez-Martinez A., Warmont F., Gloter A., Marty N., Poulain A. and Lanson B. (2015) Cryptomelane formation from nanocrystalline vernadite precursor: a high energy X-ray scattering and transmission electron microscopy perspective on reaction mechanisms. *Geochem. Trans.* **16**, 12.

Grangeon S., Lanson B. and Lanson M. (2014) Solid-state transformation of nanocrystalline phyllomanganate into tectomanganate: influence of initial layer and interlayer structure. *Acta Crystallogr., Sect. B: Struct.* **70**, 828–838.

Grangeon S., Lanson B., Lanson M. and Manceau A. (2008) Crystal structure of Ni-sorbed synthetic vernadite: a powder X-ray diffraction study. *Mineral. Mag.* **72**, 1279–1291.

Grangeon S., Lanson B., Miyata N., Tani Y. and Manceau A. (2010) Structure of nanocrystalline phyllomanganates produced by freshwater fungi. *Am. Mineral.* **95**, 1608–1616.

Grangeon S., Manceau A., Guilhermet J., Gaillot A. C., Lanson M. and Lanson B. (2012) Zn sorption modifies dynamically the layer and interlayer structure of vernadite. *Geochim. Cosmochim. Acta* **85**, 302–313.

Julien C. M., Massot M. and Poinsignon C. (2004) Lattice vibrations of manganese oxides: Part I. Periodic structures. *Spectrochim. Acta. A* **60**, 689–700.

Kim H. S., Pasten P. A., Gaillard J. F. and Stair P. C. (2003) Nanocrystalline todorokite-like manganese oxide produced by bacterial catalysis. *J. Am. Chem. Soc.* **125**, 14284–14285.

Kumagai N., Komaba S., Abe K. and Yashiro H. (2005) Synthesis of metal-doped todorokite-type MnO_2 and its cathode characteristics for rechargeable lithium batteries. *J. Power Sources* **146**, 310–314.

Kwon K. D., Refson K. and Sposito G. (2013) Understanding the trends in transition metal sorption by vacancy sites in birnessite. *Geochim. Cosmochim. Acta* **101**, 222–232.

Lanson B., Drits V. A., Feng Q. and Manceau A. (2002a) Structure of synthetic Na-birnessite: Evidence for a triclinic one-layer unit cell. *Am. Mineral.* **87**, 1662–1671.

Lanson B., Drits V. A., Gaillot A. C., Silvester E., Plançon A. and Manceau A. (2002b) Structure of heavy-metal sorbed birnessite: Part 1. Results from X-ray diffraction. *Am. Mineral.* **87**, 1631–1645.

Lanson B., Drits V. A., Silvester E. and Manceau A. (2000) Structure of H-exchanged hexagonal birnessite and its mechanism of formation from Na-rich monoclinic buserite at low pH. *Am. Mineral.* **85**, 826–838.

Llorca S. (1987) Nouvelles données sur la composition et la structure des lithiophorites d'après de échantillons de Nouvelle-Calédonie. *C. R Acad. Sci Paris - Série II* **304**, 15–18.

Llorca S. (1988) Nouvelles données sur la composition et la structure des asbolanes (Nouvelle-Calédonie). *C. R. Acad. Sci Paris - Série II* **307**, 155–161.

Loganathan P. and Burau R. G. (1973) Sorption of heavy metal ions by a hydrous manganese oxide. *Geochim. Cosmochim. Acta* **37**, 1277–1293.

Manceau A., Drits V. A., Silvester E., Bartoli C. and Lanson B. (1997) Structural mechanism of Co^{2+} oxidation by the phyllomanganate buserite. *Am. Mineral.* **82**, 1150–1175.

Manceau A., Gorshkov A. I. and Drits V. A. (1992) Structural Chemistry of Mn, Fe Co, and Ni in Mn hydrous oxides. II. Information from EXAFS spectroscopy, electron and X-ray diffraction. *Am. Mineral.* **77**, 1144–1157.

Manceau A., Kersten M., Marcus M. A., Geoffroy N. and Granina L. (2007) Ba and Ni speciation in a nodule of binary Mn oxide phase composition from Lake Baikal. *Geochim. Cosmochim. Acta* **71**, 1967–1981.

Manceau A., Lanson M. and Takahashi Y. (2014) Mineralogy and crystal chemistry of Mn, Fe Co, Ni and Cu in a deep-sea pacific polymetallic nodule. *Am. Mineral.* **99**, 2068–2083.

Manceau A., Llorca S. and Calas G. (1987) Crystal chemistry of cobalt and nickel in lithiophorite and asbolane from New Caledonia. *Geochim. Cosmochim. Acta* **51**, 105–113.

Manceau A., Marcus M. A. and Grangeon S. (2012) Determination of Mn valence states in mixed-valent manganates by XANES spectroscopy. *Am. Mineral.* **97**, 816–827.

Manceau A., Marcus M. A. and Tamura N. (2002) *Quantitative speciation of heavy metals in soils and sediments by synchrotron X-ray techniques*. Springer, pp. 341–428.

Manceau A., Marcus M. A., Tamura N., Proux O., Geoffroy N. and Lanson B. (2004) Natural speciation of Zn at the micrometer scale in a clayey soil using X-ray fluorescence, absorption, and diffraction. *Geochim. Cosmochim. Acta* **68**, 2467–2483.

Marcus M. A., Manceau A. and Kersten M. (2004) Mn, Fe, Zn and As speciation in a fast-growing ferromanganese marine nodule. *Geochim. Cosmochim. Acta* **68**, 3125–3136.

McKeown D. A. and Post J. E. (2001) Characterization of manganese oxide mineralogy in rock varnish and dendrites using X-ray absorption spectroscopy. *Am. Mineral.* **86**, 701–713.

McNeil V. H. and Cox M. E. (2000) Relationship between conductivity and analysed composition in a large set of natural surface-water samples, Queensland, Australia. *Environ. Geol.* **39**, 1325–1333.

Murray J. W. (1975) The interaction of cobalt with hydrous manganese dioxide. *Geochim. Cosmochim. Acta* **39**, 635–647.

Murray J. W., Balistrieri L. S. and Paul B. (1984) The oxidation state of manganese in marine sediments and ferromanganese nodules. *Geochim. Cosmochim. Acta* **48**, 1237–1247.

Murray J. W. and Dillard J. G. (1979) The oxidation of cobalt(II) adsorbed on manganese dioxide. *Geochim. Cosmochim. Acta* **43**, 781–787.

Nicolas-Tolentino E., Tian Z. R., Zhou H., Xia G. G. and Suib S. L. (1999) Effects of Cu^{2+} ions on the structure and reactivity of todorokite-and cryptomelane-type manganese oxide Octahedral molecular sieves. *Chem. Mater.* **11**, 1733–1741.

Onda A., Hara S., Kakiyoshi K. and Yanagisawa K. (2007) Synthesis of manganese oxide octahedral molecular sieves containing cobalt, nickel, or magnesium, and the catalytic properties for hydration of acrylonitrile. *Appl. Catal. A* **321**, 71–78.

Ostwald J. (1984) Two varieties of lithiophorite in some Australian deposits. *Mineral. Mag.* **48**, 383–388.

Ostwald J. (1986) Some observations on the chemical composition of todorokite. *Mineral. Mag.* **50**, 336–340.

Peacock C. L. (2009) Physiochemical controls on the crystal-chemistry of Ni in birnessite: genetic implications for ferromanganese precipitates. *Geochim. Cosmochim. Acta* **73**, 3568–3578.

Peacock C. L. and Sherman D. M. (2007a) Crystal-chemistry of Ni in marine ferromanganese crusts and nodules. *Am. Mineral.* **92**, 1087–1092.

Peacock C. L. and Sherman D. M. (2007b) Sorption of Ni by birnessite: Equilibrium controls on Ni in seawater. *Chem. Geol.* **238**, 94–106.

Peña J., Kwon K. D., Refson K., Bargar J. R. and Sposito G. (2010) Mechanisms of nickel sorption by a bacteriogenic birnessite. *Geochim. Cosmochim. Acta* **74**, 3076–3089.

Post J. E. (1999) Manganese oxide minerals: crystal structures and economic and environmental significance. *Proc. Natl. Acad. Sci. U. S. A.* **96**, 3447–3454.

Post J. E. and Appleman D. E. (1988) Chalcophanite, $ZnMn_3O_7$-$3H_2O$: New crystal-structure determinations. *Am. Mineral.* **73**, 1401–1404.

Post J. E. and Appleman D. E. (1994) Crystal structure refinement of lithiophorite. *Am. Mineral.* **79**, 370–374.

Post J. E., Heaney P. J. and Hanson J. (2003) Synchrotron X-ray diffraction study of the structure and dehydration behaviour of todorokite. *Am. Mineral.* **88**, 142–150.

Ravel B. and Newville M. (2006) Athena and Artemis: interactive graphical data analysis using ifeffit. *Phys. Scripta* **115**, 1007–1010.

Remucal C. K. and Ginder-Vogel M. (2014) A critical review of the reactivity of manganese oxides with organic contaminants. *Environ. Sci. Proc. Impacts* **16**, 1247–1266.

Saito M. A. and Moffett J. W. (2002) Temporal and spatial variability of cobalt in the atlantic ocean. *Geochim. Cosmochim. Acta* **66**, 1943–1953.

Saratovsky I., Gurr S. J. and Hayward M. A. (2009) The structure of manganese oxide formed by the fungus *Acremonium* sp. strain kr21-2. *Geochim. Cosmochim. Acta* **73**, 3291–3300.

Shen X. F., Ding Y. S., Liu J., Cai J., Laubernds K., Zerger R. P., Vasiliev A., Aindow M. and Suib S. L. (2005) Control of nanometer-scale tunnel sizes of porous manganese oxide octahedral molecular sieve nanomaterials. *Adv. Mater.* **17**, 805–809.

Shen Y. F., Suib S. L. and O'Young C. L. (1994) Effects of inorganic cation templates on octahedral molecular sieves of manganese oxide. *J. Am. Chem. Soc.* **116**, 11020–11029.

Siegel M. D. and Turner S. (1983) Crystalline todorokite associated with biogenic debris in manganese nodules. *Science* **219**, 172–174.

Silvester E., Manceau M. and Drits V. A. (1997) Structure of synthetic monoclinic Na-rich birnessite and hexagonal birnessite: II. Results from chemical studies and EXAFS spectroscopy. *Am. Mineral.* **82**, 962–978.

Simanova A. A. and Peña J. (2015) Time-resolved investigation of cobalt oxidation by Mn (III)-rich δ-MnO$_2$ using quick X-ray absorption spectroscopy. *Environ. Sci. Technol.* **49**, 10867–10876.

Song C., Li R., Liu F., Feng X., Tan W. and Qiu G. (2010) Cobalt-doped todorokites prepared by refluxing at atmospheric pressure as cathode materials for Li batteries. *Electrochim. Acta* **55**, 9157–9165.

Taylor R. M. (1968) The association of manganese and cobalt in soils—further observations. *Eur. J. Soil Sci.* **19**, 77–80.

Taylor R. M., McKenzie R. M. and Norrish K. (1964) The mineralogy and chemistry of manganese in some Australian soils. *Aust. J. Soil Res.* **2**, 235–248.

Tebo B. M., Bargar J. R., Clement B. G., Dick G. J., Murray K. J., Parker D., Verity R. and Webb S. M. (2004) Biogenic manganese oxides: Properties and mechanisms of formation. *Annu. Rev. Earth Pl. Sci.* **32**, 287–328.

Villalobos M., Bargar J. and Sposito G. (2005) Mechanisms of Pb (II) Sorption on a Biogenic Manganese Oxide. *Environ. Sci. Technol.* **39**, 569–576.

Villalobos M., Lanson B., Manceau A., Toner B. and Sposito G. (2006) Structural model for the biogenic Mn oxide produced by *Pseudomonas putida*. *Am. Mineral.* **91**, 489–502.

Vodyanitskii Y. N., Vasilev A. A., Lesovaya S. N., Sataev E. F. and Sivtsov A. V. (2004) Formation of manganese oxides in soils. *Eurasian Soil Sci.* **37**, 572–584.

Webb S. M., Tebo B. M. and Bargar J. R. (2005) Structural characterization of biogenic Mn oxides produced in seawater by the marine *Bacillus* sp. strain SG-1. *Am. Mineral.* **90**, 1342–1357.

Yin Y. G., Xu W. Q., Shen Y. F., Suib S. L. and O'Young C. L. (1994) Studies of oxygen species in synthetic todorokite-like manganese oxide octahedral molecular sieves. *Chem. Mater.* **6**, 1803–1808.

Yin H., Li H., Wang Y., Ginder-Vogel M., Qiu G., Feng X., Zheng L. and Liu F. (2014) Effects of Co and Ni co-doping on the structure and reactivity of hexagonal birnessite. *Chem. Geol.* **381**, 10–20.

Yin H., Liu F., Feng X., Hu T., Zheng L., Qiu G., Koopal L. K. and Tan W. F. (2013) Effects of Fe doping on the structures and properties of hexagonal birnessites – comparison with Co and Ni doping. *Geochim. Cosmochim. Acta* **117**, 1–15.

Yin H., Liu Y., Koopal L. K., Feng X., Chu S., Zhu M. and Liu F. (2015) High Co-doping promotes the transition of birnessite layer symmetry from orthogonal to hexagonal. *Chem. Geol.* **410**, 12–20.

Yu Q., Sasaki K., Tanaka K., Ohnuki T. and Hirajima T. (2012) Structural factors of biogenic birnessite produced by fungus *Paraconiothyrium*, sp. wl-2 strain affecting sorption of Co^{2+}. *Chem. Geol.* **310–311**, 106–113.

Zhao H., Liang X., Yin H., Liu F., Tan W., Qiu G. and Feng X. (2015) Formation of todorokite from "c-disordered" H$^+$-birnessites: the roles of average manganese oxidation state and interlayer cations. *Geochem. Trans.* **16**, 1–11.

Associate editor: Mario Villalobos